RSC Applied Interfaces

ROYAL SOCIETY OF CHEMISTRY

REVIEW

View Article Online
View Journal | View Issue

Cite this: *RSC Appl. Interfaces*, 2025, **2**, 1507

Recent advances in interface engineering of bismuth-based materials for photocatalytic CO_2 reduction

Swetha S. M. Bhat * and Girish Kumar S.

Received 26th May 2025,
Accepted 13th August 2025

DOI: 10.1039/d5lf00154d

rsc.li/RSCApplInter

Photocatalytic reduction of CO_2 into value-added products is witnessed as a promising technology to mitigate global warming and energy crisis. Among the illustrious functional semiconductors, bismuth-based materials are feasible for the CO_2 reduction reaction owing to their convenient preparation, their narrow band gap and the availability of hybridized energy states in the conduction band. Furthermore, the inherent two dimensional (2D) layered structure of few Bi materials remains an added advantage for various photocatalytic reactions. In this focused review, the interfacial engineering of Bi-based semiconductors achieved by coupling them with distinct photocatalytic materials to form type-I, type-II, Z-scheme or S-scheme heterojunctions is discussed, and their applications in CO_2 reduction reactions are emphasized. Further advancements, including co-catalyst loading, defect engineering and designing hierarchical morphology from the perspective of improving charge carrier separation and structural stability are highlighted. The preparation methods and mechanistic pathways for the CO_2 reduction reaction are briefly summarized. Finally, the challenges and scope of Bi-based materials to spotlight their applications in energy- and environment-related areas are presented.

1 Introduction

Global energy consumption using nonrenewable fossil fuels has skyrocketed in the recent decade, leading to significant global climate changes and an imbalance in the ecosystem. As per the literature, CO_2 emissions have substantially increased by ~40% since the industrial revolution.[1,2] Therefore, the development of efficient methods to convert CO_2 into value-added products has drawn attention because they can conveniently address environmental issues and energy demands.[3] Numerous technologies such as chemical reforming, biological, electrochemical, photocatalytic, and photoelectrocatalytic processes have been extensively investigated over the years to address these issues.[4–9] Among them, photocatalytic CO_2 reduction is found to be a sustainable solution for the removal of atmospheric CO_2 and its transformation into selective gaseous (methane or ethane) and liquid-phase products (formate, methanol, or ethanol) are interesting.[10–12] Compared to other approaches, this technique benefits from superior product selectivity, economic viability and environmental benignness.[13] Linear CO_2 with sp^2 hybridized C=O bonds requires more dissociation energy than C–C and C–H bonds, and an adequate amount of energy is required to activate CO_2 molecules.[14,15] The primary step in the reduction process demands the strong adsorption of CO_2 on the catalytic surface, which is subsequently followed by its activation by surface active sites.[16–18] CO_2 photoreduction imitates the photosynthesis of plants, *i.e.*, it utilizes water and CO_2 and converts them into chemical fuels such as methane or methanol and value-added multi-carbon products. The reaction product ratio varies with the number of electrons participating in the reaction, nature of photocatalytic materials and the adopted reaction conditions.[14–18]

The primary step in semiconductor photocatalysis involves the absorption of light energy by catalysts with energy levels greater than or equal to those of their band gaps to generate electron–hole pairs. These excitons migrate towards the surface and interact with the adsorbed species to produce products *via* redox reactions, which later desorb from the surface of the catalyst.[19] As per theoretical calculations and kinetic studies, CO, COOH and COH are common intermediates in the CO_2 reduction reaction.[20] CO_2 photoreduction will proceed only when the energy of the conduction band of the concerned semiconductor is more negative than the reduction potential of the desired products.[2] Semiconductors such as BiOX, CdS, g-C_3N_4, Cu_2O, SnO_2, TiO_2, ZnO, and perovskites are extensively used for the CO_2 reduction reaction.[21–31] Bismuth-based materials have garnered major interest because they possess band gaps spanning the major portion of the solar spectrum, and their band edge positions are convenient to trigger the desired

Department of Chemistry and Centre of Excellence in Nanomaterials and Devices, RV College of Engineering, Bengaluru, Karnataka 560059, India.
E-mail: swethasm@rvce.edu

reduction and oxidation reactions.[32–37] The Bi 6s orbital hybridizes with the O 2s orbital to form a highly dispersive energy band structure, which promotes charge carrier transport and also exhibits high oxidizing capabilities. Furthermore, bismuth-based materials offer stable structures with layered spaces to promote the intercalation of foreign ions without changing their structural features. Because of their low toxicity, environmental friendliness and exceptional photostability, the distinct morphologies of bismuth-based materials have been explored for photocatalytic applications.[11,38] Different categories of bismuth-based materials such as unitary (Bi), binary (Bi_2S_3 and Bi_2O_3), and ternary (stoichiometric and non-stoichiometric bismuth oxy halides, $BiVO_4$, Bi_2WO_6, and Bi_2MoO_6) are used for photocatalytic CO_2 reduction.[36,39–41] However, the massive charge carrier recombination and narrow optical response of single-phase photocatalysts limit their performance under light-illuminated conditions.[39,42,43] Several reviews on bismuth-based materials for photocatalytic applications can be found in the literature.[37,38,41,44,45] However, the recent trend in the interfacial engineering of these materials is scarcely emphasized. Motivated by these aspects, this review summarizes the interfacial engineering of bismuth-based materials with various semiconductors under different reaction conditions, and their performance in photocatalytic CO_2 reduction is outlined.

2 Strategies for interfacial engineering

Heterojunction formation is found to be a promising method to improve the photocatalytic performance of semiconductors owing to the synergistic interactions arising from the structure–optical–morphological properties of the integrated semiconductors.[46–49] The prime requisite to fabricate a heterojunction is that the band position of the concerned semiconductors must possess different potentials to achieve the maximum separation of charge carriers.[50,51] Secondly, the bandgap response of the individual components must be substantially different so that the composite absorbs a larger fraction of the solar light for the photocatalytic reactions. Various types of heterojunctions have been fabricated for bismuth-based materials to increase the conversion efficiency of CO_2 to value-added products. Following are the methods that have been adopted extensively for various types of bismuth-based materials:

(i) Type-II heterojunction: when two semiconductors with different band edge potentials and Fermi levels encounter each other, three types of heterojunctions, namely, type-I, type-II and type-III, are formed. Type-I allows for the migration of both the charge carriers from one semiconductor to another due to their straddle bandgap configuration, which enhances charge carrier recombination (Fig. 1). In contrast, type-II is efficient in separating the electron–hole pairs due to the staggered configuration of the electronic band positions. It is also referred to as the cascade electron transfer process, as it promotes interfacial charge carrier separation. However, the potential of electrons and holes decreases, lowering the efficiency of the composite.

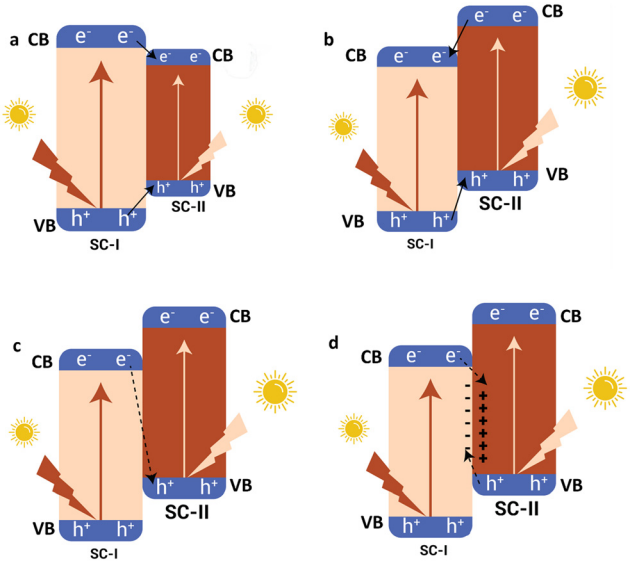

Fig. 1 Different types of semiconductor–semiconductor heterojunctions: a) type-I, b) type-II, c) Z-scheme, and d) S-scheme heterojunctions. Note: SC = semiconductor; CB = conduction band; VB = valence band.

(ii) Z-scheme: though type-II heterojunctions can improve the photocatalytic activity, they suffer from the recombination of electrons and holes. This disadvantage can be avoided by the Z-scheme technique.[52]

The band gap configuration in the Z-scheme is similar to the type-II configuration, but an exception remains in the direction of electron transfer pathways. The low-potential electrons accumulated on one side of the semiconductor recombine with the low-potential holes of another semiconductor, thereby retaining the high-potential electrons and holes for the redox reactions.

Although significant improvement can be observed from Z-scheme photocatalysis, this technique fails to deliver superior photocatalytic performance as the limitation arises from the choice of the semiconductors.[53]

(iii) S-scheme heterojunction: the step scheme (S-scheme) was introduced by the Jiaguo Yu group.[54,55] When reduction and oxidation photocatalysts are in close contact, the electrons in the oxidation photocatalyst recombine with holes present in the valence band of the reduction photocatalyst. Positive and negative charges are formed at reduction and oxidation photocatalysts, respectively, and the direction of the in-built electric field is from the reduction photocatalyst to the oxidation photocatalyst. Thus, electron depletion at the reduction photocatalyst causes the upward band bending, and electron accumulation at the oxidation photocatalyst results in the downward band bending. Driven by the rise of the electric field and Coulombic force of attraction, the electrons in the oxidation photocatalyst recombine with holes in the reduction photocatalyst while preserving the energetic charge carriers for the desired redox reactions.[55] The

preserved electrons and holes are available for the reaction to take place, making the photocatalytic system more efficient than type-II and Z-scheme heterojunctions. The positions of the conduction and valence bands for different bismuth-based materials clearly signify their ability to participate in the CO_2 reduction reactions (Fig. 2).

(iv) Cocatalyst loading: cocatalysts such as noble metals, which include Pt, Ag and Au, non-noble metals, such as Bi, Cu, and Mg, have been exploited to improve the performance of the photocatalytic process.[56–58] The activation energy required to convert CO_2 to any value-added product can be reduced by the addition of cocatalysts on the semiconductor surface. It is also found from the literature that it increases reaction sites and plays a vital role in determining the selectivity, adsorption of CO_2, and photostability of the photocatalyst.[59,60]

(v) Defect engineering: defects are of paramount importance in tailoring the bandgap and charge carrier dynamics of functional semiconductors. In general, anionic vacancies like oxygen vacancies can narrow the gap region and shift the optical response of the host matrix to the visible region. Few reports also hint that the tailoring the bandgap depends on the density of oxygen vacancies in the host matrix.[61,62] Furthermore, oxygen vacancies can trap charge carriers to restrain their recombination with holes and extend the charge carrier lifetime. On the contrary, cationic vacancies can temporarily trap holes. In recent times, the vacancy-rich Bi-based materials are reported to show superior photocatalytic activity compared to their low-defect counterparts.[45,63,64] These defects can alter lattice strain and surface defects, which can facilitate the adsorption of oxygen to promote the formation of superoxide radicals in the solution phase.[65]

3 Bi-based semiconductors

3.1 BiOX

BiOX is highly crystalline with a tetragonal crystal structure and is extensively used for photocatalytic applications owing to its layered structure and narrow band gap.[66] It is composed of a layered structure with $[Bi_2O_2]$ slabs and two arrays of $[X]^-$ ions. The exciton pairs can be effectively separated because the charge density is higher in Bi–O than in [X] slabs. In addition, the static electric field along the *c*-axis avoids massive charge carrier recombination pathways.[67] BiOCl is an indirect band gap semiconductor, which decreases the chance of the recombination of charge carriers.[68–71] Defects in BiOX can influence the photocatalytic activity by modifying the charge transport and electronic structure of the material. The oxygen vacancy can be introduced easily to BiOCl because the Bi–O bond is weak. These oxygen vacancies can increase the number of active sites to facilitate the CO_2 adsorption and activation processes.[72] It has been observed that the majority of BiOX-based heterojunctions produce only CO and CH_4, and therefore, the interfacial engineering of BiOX plays a crucial role in improving the selectivity.[73] The crystal facet of BiOCl also influences the photocatalytic activity when coupled with CdS. CdS/BiOCl with an exposed {001} facet exhibited higher performance than {010} facets.[67] This was attributed to the effective coupling of the interfacial electric field of the heterojunction and the polarization electric field of the {001} crystal facet of BiOCl. The production of CH_4 and CO with {001}-BiOCl/CdS was higher than that with {010}-BiOCl/CdS, even though the bandgap energy and band edge potential of both the facets were almost similar. This result suggests that the crystal facet orientation of BiOCl has a profound influence on the adsorption and activation of CO_2. As the polarization electric field for BiOCl is along the *c*-axis, excited electrons easily accumulate on the {001} facet, which favours their recombination with the valence band holes of CdS, thereby improving the energetic electrons and holes from CdS and BiOCl, respectively, to participate in the redox reactions.[67] The 2D/2D Vo–WO_x/BiOCl S-scheme was fabricated by a self-assembly process. The S-scheme heterojunction not only offered the separation of photogenerated charge carriers but also provided a dual interfacial pathway to improve the charge separation

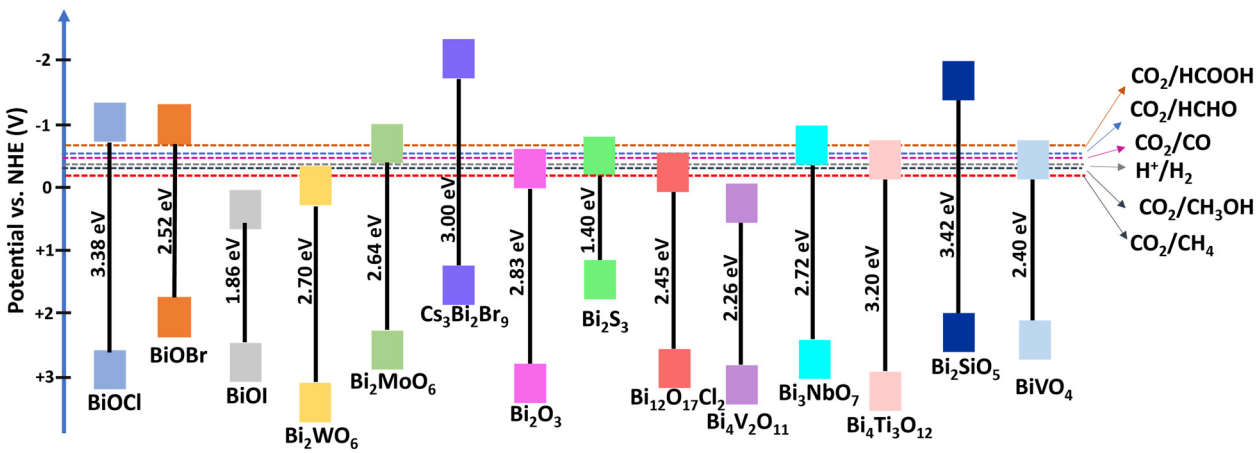

Fig. 2 Band positions of different bismuth-based semiconductors.

process.[74] Jiang *et al.* showed that CO_2 molecules were adsorbed on BiOCl (001) and WO_x (010) surfaces.[75] The study also suggested that CO_2 molecules were more stable on the surface of BiOCl than that of WO_x. The conduction band level of WO_x was not sufficient to carry out the reduction of CO_2 molecules. As a result, the adsorption and reaction sites were available only on the surface of BiOCl.[75] Similarly, Bi_2WO_6 was also used to fabricate a heterojunction with BiOCl. Unlike the S-scheme in WO_x/BiOCl, they formed a typical type-II heterojunction. Theoretical calculations confirmed that the production of the CHO* intermediate on the surface of BiOCl/Bi_2WO_6 was responsible for the selective generation of CH_4. The high selectivity towards CH_4 was due to the ultrathin nanosheet morphology (2D/2D) and the presence of an internal electric field at the heterointerface.[76] BiOCl/In_2O_3 fabricated by the hydrothermal method with a type-II heterojunction yielded a high rate of CO_2 photoreduction.[77] This enhanced performance was attributed to the narrow band gap, which falls in the visible region. In another report, a chlorophyll and Mg co-modified BiOCl (Chl–Mg/BiOCl) microsphere exhibited superior photocatalytic applications. Chl–Mg/BiOCl yielded 100 μmol g^{-1} of CH_4. The chlorophyll on the surface of the BiOCl produced singlet states of Chl–Mg*, which acted as an electron donor. Mg formed a complex with chlorophyll and helped to improve the stability of the catalyst.[78]

It is also noted that the cocatalyst loading on the photocatalyst is a potential approach to improve the adsorption of the intermediates during CO_2 reduction, thereby influencing the coupling of the C–C bond. To improve C_2 hydrocarbon selectivity and to enhance the photocatalytic reduction of CO_2, transition metal cocatalysts with nanostructures were loaded on BiOCl.[71,79,80] The selectivity towards CH_4 was increased by decorating noble metals, such as Pd, on BiOCl. Pd not only decreased the recombination of the charge carriers but also changed the intermediate formed (from HCO_3^- to HCOO* and CH_3O*; CH_3O* will be reduced to CH_4) on the surface of BiOCl.[80]

In situ diffused reflectance infrared Fourier transform (DRIFT) spectroscopy revealed that the key intermediates were bidentate formate and methoxy, which promote the selectivity for CH_4 production.[80] The photocatalytic activity of ultrathin BiOCl sheets can be altered by introducing magnetically active metal particles. In this context, Li *et al.*

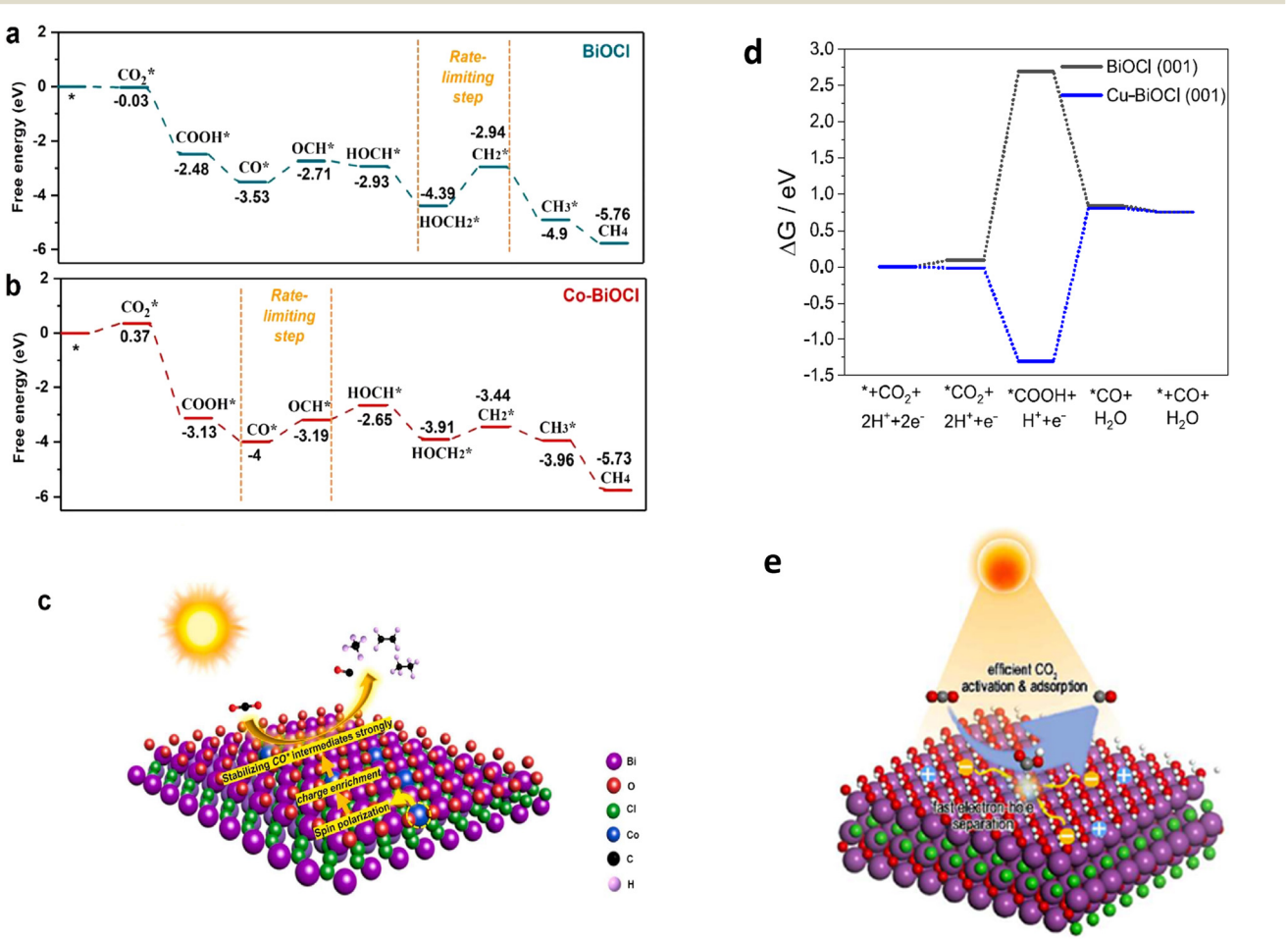

Fig. 3 Computed Gibbs free energy main reactions for the photocatalytic reduction of CO_2 on a) pristine BiOCl and b) Co–BiOCl.[79] c) CO_2 reduction pathway on the surface of Co-BiOCl. d) Gibbs free energy diagram for CO_2 reduction on Cu–BiOCl. e) Scheme for the photoreduction of CO_2 to CO. Reproduced with permission from ref. 68. Copyright 2022, American Chemical Society and ref. 79. Copyright 2024, Elsevier.

reported that Co-doped BiOCl selectively converted CO_2 to CH_4 and C_{2+} products, which was not possible with the pristine BiOCl. The increase in the photocatalytic activity was due to the Co–O bond on the Co–BiOCl.[79] The increased CO_2 adsorption was primarily responsible for the enhanced CO_2 photoreduction. It was also found that the introduction of Co on BiOCl generated spin-polarized charges and changed the intermediate formed on the surface of BiOCl. In order to generate CH_4 and C_{2+} products, the CO* intermediate would be formed *via* the formation of the COOH* intermediate (Fig. 3a–c). The rate-limiting step for Co–BiOCl was the conversion of CO* to CHO*, whereas for BiOCl, $HOCH_2^*$ to CH_2^* was the rate-limiting step.[79] This work showed that the spin polarization of the charge on the surface of BiOCl resulted in the formation of a stable intermediate and promoted C–C coupling to yield CH_4 and C_{2+} products. Similarly, Cu was modified on BiOCl nanosheets, which resulted in surface charge distribution. Cu–BiOCl improved the catalytic performance and enhanced the absorption of light.[71] Also, it decreased the activation energy barrier, which facilitates the faster consumption of CO_2 molecules, resulting in an increased CO yield (Fig. 3d and e). Metal cocatalysts, such as Pt, Pd and Au metals, have been decorated on BiOCl nanostructures by the deposition–precipitation method. The main product obtained with BiOCl was CO, while CH_4 production dominated after loading the metal cocatalyst.[81]

Chen *et al.* demonstrated that Z-scheme In_2S_3/BiOCl could be prepared by solution combustion synthesis. The nanopetals of BiOCl were decorated on the nanoflowers of In_2S_3 *via* solution combustion synthesis. In_2S_3/BiOCl nanostructures were evenly deposited on the surface of MnO_2 nanowires.[82] Initially, In_2S_3 nanoflowers were synthesized by the hydrothermal approach. The synthesized In_2S_3 nanoflowers were dissolved in thiourea, a bismuth nitrate precursor and concentrated nitric acid and stirred vigorously. To this solution, urea and ammonium chloride were added and stirred constantly for 24 h. The In_2S_3/MnO_2/BiOCl was fabricated by using the suspension of In_2S_3/BiOCl by the hydrothermal approach. Despite having higher solubility than In_2S_3, BiOCl grew on the surface of In_2S_3.[82] In_2S_3/BiOCl deposited uniformly on MnO_2 nanowires, which formed an assembly of hierarchical structures. It is noted from this work that the S^{2-} ions play a significant role in controlling the nucleation of In_2S_3, forming the morphology and controlling the size of the nanostructure. This ternary heterojunction exhibited photocatalytic reduction rates of 51.2 μmol g^{-1} h^{-1} for CO_2 to CO, 63.2 μmol g^{-1} h^{-1} for CO_2 to C_2H_4, and 42.4 μmol g^{-1} h^{-1} for CO_2 to CH_4 conversion.[82] The observed synergistic effect was attributed to the Mn 3d electrons, which have narrowed the band gap. The key intermediates of the photocatalytic reduction were CHO* and COOH* for the production of CO, CH_4 and C_2H_4.[83] BiOCl with a BiOBr heterojunction was fabricated by the mechanical method, which yielded the type-I heterojunction.[84] This heterojunction reduced CO_2 to CO with a formation rate of 7.353 μmol g^{-1} h^{-1}.

The $CsPbBr_3$ perovskite is attracting increasing attention owing to its visible light harvesting capability, and its high conduction band position enhances the reduction capability.[85] Various heterojunctions have been constructed based on the $CsPbBr_3$ perovskite because the pristine material suffers from severe recombination of charge carriers. A 2D/2D S-scheme heterojunction comprising BiOCl and $CsPbBr_3$ was fabricated by an efficient self-assembly method. The zeta potential measurements revealed the negative and positive surface charge densities on BiOCl and $CsPbBr_3$, which could adhere to each other *via* electrostatic forces of attraction. The nanosheets of the perovskite were assembled on the nanosheets of BiOCl, which provided face-to-face contact, and a strong interfacial area existed between them. This heterojunction afforded much improved photocatalytic activity towards CO_2 reduction to form CO as the major product and CH_4 as a minor product.[85] The high content of $CsPbBr_3$ in the composite reduced the CO production, while the yield of CH_4 remained almost the same irrespective of its content.[85]

Chen *et al.* synthesized BiOCl by the hydrothermal method, and the oxygen vacancy was introduced by heating at 60 °C in a vacuum oven.[86] The Z-scheme heterostructure was fabricated by vigorously stirring powders of BiOCl with oxygen vacancies and 2D g-C_3N_4 nanosheets in an ultrasonic bath. It was found that the heterojunction could be constructed effectively if the two individual components were stirred in an ultrasonic bath rather than on a magnetic stirrer.[86] The authors observed that the photocatalytic reduction of CO_2 to CO on the interfacial oxygen-vacancy induced g-C_3N_4/BiOCl heterostructure was 1.6 times higher than that on the pristine g-C_3N_4/BiOCl.

Ternary composites of BiOCl with dual Z-schemes of BiOCl/g-C_3N_4/Ag_2CrO_4 have also been synthesized and found to give CO and CH_4 with yields of 30.20 and 81.21 μmol g^{-1}, respectively.[87] It is possible to make a ternary heterojunction with C_3N_4 and BiOCl using the Ag_2CrO_4 photocatalyst. The dual Z-scheme heterojunction photocatalyst was synthesized by a simple method. BiOCl/C_3N_4 was prepared by taking the Bi, C and N precursors and heating solvothermally using ethylene glycol as the solvent for 12 h at 140 °C. However, the BiOCl/C_3N_4/Ag_2CrO_4 was synthesized by stirring the powders of BiOCl/C_3N_4 and precursors of Ag^+ and Cr^{6+} ions for 2 h. When the ternary heterojunction was formed, the morphologies of BiOCl, C_3N_4 and Ag_2CrO_4 were retained. The irregular shapes of Ag_2CrO_4 were uniformly decorated on the microspheres of BiOCl and the nanosheets of C_3N_4. It was observed that C_3N_4 provided charge transfer pathways to form dual Z-scheme heterojunctions.

$MgIn_2S_4$ is another chalcogenide that exhibits a promising band gap and photostability and is extensively used for the removal of liquid pollutants and for the production of

hydrogen.[88] Zhang *et al.* fabricated an S-scheme heterojunction of Bi–BiOCl/$MgIn_2S_4$ by the hydrothermal technique and $NaBH_4$ reduction technique.[89] The microspheres of BiOCl with an average diameter of 1 μm were obtained by the hydrothermal method, and Bi self-doped BiOCl was synthesized by treating BiOCl microspheres with $NaBH_4$, followed by vacuum drying. Bi–BiOCl/$MgIn_2S_4$ was synthesized by the *in situ* hydrothermal method, and the obtained product exhibited ultrathin sheets of BiOCl dispersed on the surface of $MgIn_2S_4$ marigold flowers. It was noted that $NaBH_4$, which was used as a reducing agent, influenced the morphology of BiOCl and caused the rough surfaces and loose internal structures.[89] The formed S-scheme heterojunction exhibited the conversion of CO_2 to CH_4 with a yield of 25.72 μmol g^{-1}.

BiOBr exhibits an appropriate band structure, making it suitable for photocatalytic applications. However, the performance of BiOBr needs band-structure modification, as it promotes electron–hole recombination. The g-C_3N_4 has a band gap that falls in the visible light wavelength, and therefore, coupling it with BiOBr would help utilize a larger fraction of solar light.[90] The hollow microspherical morphology of BiOBr was completely destroyed when grown on the surface of g-C_3N_4 sheets *via* the wet-chemical approach. The composite selectively produced CH_3OH from CO_2 at the optimized content of g-C_3N_4.[90] Liu *et al.* synthesized BiOBr/C_3N_4 by ultrasonicating the synthesized BiOBr and C_3N_4 for 6 h.[91] BiOBr was synthesised by the solvothermal technique, and the oxygen vacancy was introduced by adding the surfactant along with precursors. Furthermore, oxygen vacancies could be introduced to BiOBr by adding the surfactant during solvothermal synthesis, which is not possible during hydrothermal synthesis. The g-C_3N_4 heterojunction was constructed with BiOBr possessing surface oxygen vacancies. The morphology has been compared in Fig. 4.[91] Along with the heterojunction interface, the presence of surface oxygen vacancies promoted the charge separation, and hence, the photocatalytic performance was enhanced.

Xi *et al.* also synthesized BiOBr/Bi_2S_3 and conducted a detailed analysis on the growth mechanism of Bi_2S_3 nanoarrays on BiOBr nanoplates.[92] The facet-sensitive growth of Bi_2S_3 can be used as an effective strategy to construct a heterojunction with an increased number of active sites using thioacetamide as the sulfur source. It can also be observed

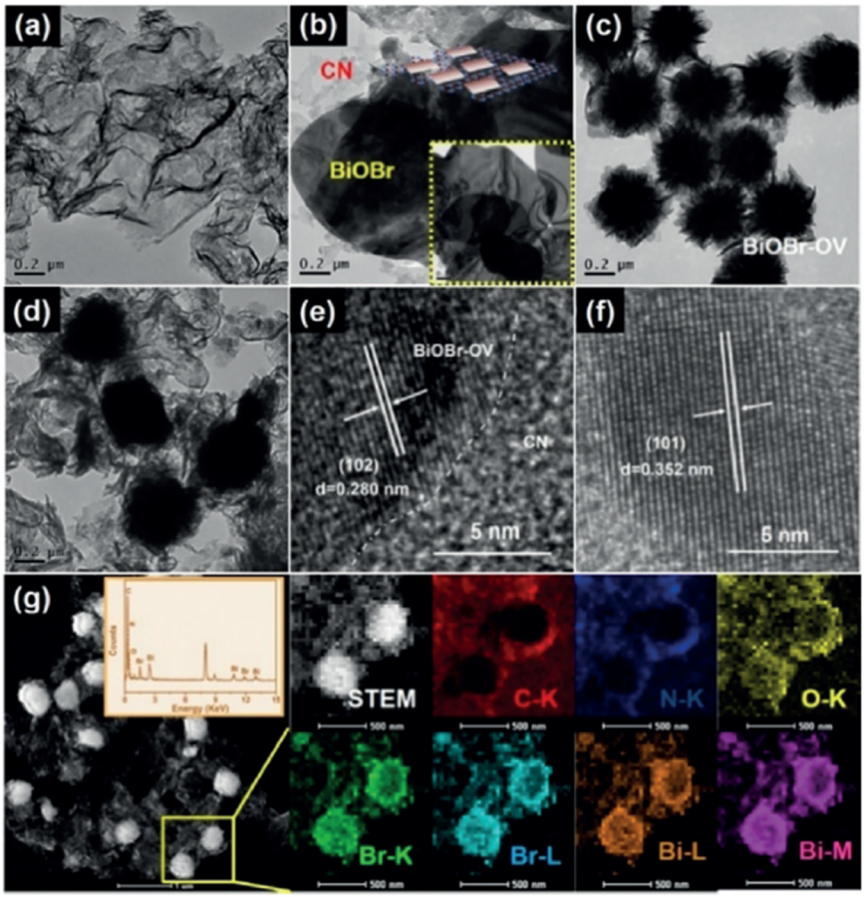

Fig. 4 Transmission electron microscopy (TEM) images of a) pure C_3N_4 (CN), b) CN–BiOBr and BiOBr (marked in the lower right corner), c) bare BiOBr–OV, and d) the CN–BiOBr–OV catalyst. e) and f) High resolution (HR)-TEM images of the CN–BiOBr–O_V heterojunction with the lattice spacings, and g) elemental maps of C, N, O, Br, and Bi in the CN BiOBr–O_V photocatalyst. Reproduced with permission from ref. 91. Copyright 2020, Wiley-VCH.

that the structurally a very close matching of the lattice parameters between *c*-axis of Bi_2S_3 and *a* or *b* axis of BiOBr facilitates the selective growth of Bi_2S_3 facets.[92] The established S-scheme heterointerface between BiOBr and Bi_2S_3 produced 20.32 μmol g^{-1} CO from CO_2 photoreduction.[92] The large area exposure of both semiconductors helped in exploiting the maximum amount of visible light. Directional growth of mesh like Bi_2S_3 nanostructure as grown on the surface of BiOBr nanoplates *via* topotactic transformation process found to be effective in enhancing the photocatalytic activity.[92]

Vertically aligned Bi_2S_3 nanowalls helped in the minimal shielding of the light falling on the surface of the BiOBr nanoplate substrate, which extended the optical response to 1000 nm (Fig. 5). The authors demonstrated that the vacancy-rich BiOBr substrate enhanced the adsorption of CO_2 on the surface.[92] Due to the weak Bi-O linkage, it was easy to produce oxygen vacancies in BiOBr. Because oxygen vacancies created trap centres for photogenerated charge carriers, it enhanced the separation efficiency. The rational design of oxygen-vacancy rich BiOBr heterojunctions would be beneficial in elevating the photocatalytic CO_2 reduction.

Ma *et al.* suggested that instead of constructing conventional heterostructures, co-sharing atoms can be an effective strategy for interfacial engineering along with a suitable band structure. This work stresses the atom-level interfacial contact of the heterostructures.[93] BiOBr was coupled with a Bi_2S_3 layered structure to deliver a full-spectrum responsive S-scheme photocatalyst. BiOBr/Bi_2S_3 was fabricated by an *in situ* ion exchange method, which yielded Bi_2S_3 nanorods on BiOBr nanosheets. It was observed that the morphology of BiOBr nanosheets changed after reacting with sulfur atoms during the hydrothermal reaction, which indicates that the occurrence of the ion exchange reaction led to the formation of the heterojunction. It was also noted that as the sulfur concentration increases, the density of Bi_2S_3 nanorods on BiOBr nanosheets. The BiOBr/Bi_2S_3 heterostructure yielded 20.32 μmol g^{-1} CO.

Bi_2WO_6 has a layered structure comprising fluorite-like $[Bi_2O_2]^{2+}$ and perovskite-like $[WO_4]^{2-}$. Owing to the strong oxidising capability of its valence band, Bi_2WO_6 is extensively studied for photocatalytic applications. However, the performance is limited by the severe recombination of the photogenerated charge carriers. Therefore, a composite of Bi_2WO_6 and BiOBr would enhance the photocatalytic conversion of CO_2 reduction.[94] It is known from the literature that surface oxygen vacancies can easily be created on Bi_2WO_6 and BiOBr, which can provide an increased number of adsorption sites for the reactants and trap states for the photogenerated charge carriers.[68,95] Apart from oxides and sulfides, layered double hydroxides (LDHs) have also been used for making composites with BiOBr. CoAl-LDH has high selectivity towards CH_4, whereas NiAl-LDH yields CO.[96] As CoAl-LDH has suitable band positions with BiOBr, facile electron–hole pair separation is possible. The heterojunction was fabricated by the hydrothermal method. The optimal amount of ultrathin CoAl-LDH loaded on BiOBr improved the selectivity towards CH_4, a value-added chemical.[96] In most of the cases, pristine BiOBr yields CO *via* photocatalytic conversion. In order to obtain value-added products such as CH_4, the p-type semiconductor Cu_2O was heterojunctioned with BiOBr.[97] Recent studies have found that using metallic Bi is beneficial for enhancing the photogenerated charge separation.[14,98,99] Many reports claim that Bi–BiOBr shows enhanced performance towards CO_2 photoreduction.[100] Abundant oxygen vacancies can be successfully synthesized by the *in situ* partial ion-exchange method on the heterojunction materials.[74] More importantly, metallic Bi self-doped Bi_2SiO_5 synthesized by the hydrothermal method can provide a facile situation for S-scheme heterojunctions and thereby increase the redox capability in the S-scheme BiOBr-(001)/Bi_2SiO_5/Bi heterojunction, which gives a CO production rate of 234.05 μmol g^{-1} h^{-1}.[74]

AgBr is another excellent photo-responsive material, but it suffers from instability due to the reduction of silver ions to metallic silver upon exposure to light. The low electron–hole recombination and extended visible light response were achieved in BiOBr/AgBr.[101] Density functional theory and experimental results demonstrated that an electron depletion region is produced on BiOBr, whereas electrons accumulate on AgBr, resulting in an S-scheme heterojunction to produce CO and CH_4. As the intensity of the light increases, the production of CO and CH_4 increases linearly, proving that the reaction follows first-order kinetics.[101] $BiOBr_xI_{1-x}$ was coupled with $BiPO_4$ to form a p–n junction, which was synthesized by the solvothermal method.[102] This heterojunction exhibited increased photocatalytic activity compared to $BiPO_4$.[102] The 0D/2D $CsPbBr_3$/BiOBr grown under different conditions selectively produced CO rather than CH_4.[103,104] The oxygen vacancies in BiOBr modulated the adsorption and activation of CO_2, and the highly negative conduction band position of quantum dots (QDs) promoted the reduction reaction pathways. Recently, the coupling of BiOBr with p-type NiO was reported to be active for CO_2 reduction to yield CO and CH_4.[105] It was proposed that the adsorption of CO_2 on the composite surface formed carbonate species, which were converted to formic acid by capturing protons and electrons. The formic acid was successively transformed to

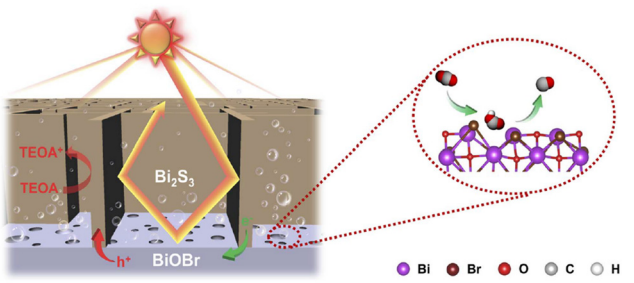

Fig. 5 Schematic illustrating the proposed mechanism for photocatalytic CO_2 reduction over the BiOBr/Bi_2S_3 heterojunction. Reproduced with permission from ref. 92. Copyright 2022, Royal Society of Chemistry.

formaldehyde, methanol and methane by continuous hydrogenation processes. Alternatively, CO_2 was directly transformed into CO by hydrogenation and dehydration.[105] The conduction band of NiO is mainly derived from the orbitals of Ni, which enables the accumulation of electrons at the Ni sites of NiO, which primarily serve as adsorption centres for CO_2.[105]

Among BiOX materials, BiOI exhibits the narrowest band gap (~1.6 to 1.9 eV), which enhances the absorption of light in the visible region. BiOI consists of alternative layers of $[Bi_2O_2]$ and iodine held by van der Waals forces of attraction. BiOI, an indirect band gap semiconductor, was heterojunctioned with a perovskite material to improve the interfacial charge separation. The direct band gap semiconductor cesium formamidinium lead halide perovskite ($Cs_{1-x}FA_xPbBr_3$) was coupled with BiOI nanosheets.[106] It is worth noting that the heterojunction was created by stirring the solution of BiOI and perovskite nanocrystals owing to the low surface energy of perovskite nanocrystals and strong interactions between Bi cations and perovskite Br anion. The perovskite with a cuboid structure was well decorated on the ultrathin nanosheets of BiOI, as confirmed by SEM and TEM images. The authors demonstrated the kinetic models, as shown in Fig. 6, and they claim that BiOI had more surface defects than the perovskite $Cs_{1-x}FA_xPbBr_3$ (CF).[106] However, when BiOI and CF were heterojunctioned, the blue side of the photoinduced absorption band (PIA) allowed transition with Bi^{3+} doping in CF. An internal electric field (IEF) was created due to the electron transfer between BiOI and CF, which facilitates the recombination of electrons from the conduction band of BiOI and the holes from the valence band of the CF perovskite to form an S-scheme heterojunction, as depicted in Fig. 6.

The formation of the S-scheme was confirmed by X-ray photoelectron spectroscopy. Femtosecond transient absorption spectroscopy was utilized to investigate the ultra-rapid dynamics of charge carriers.

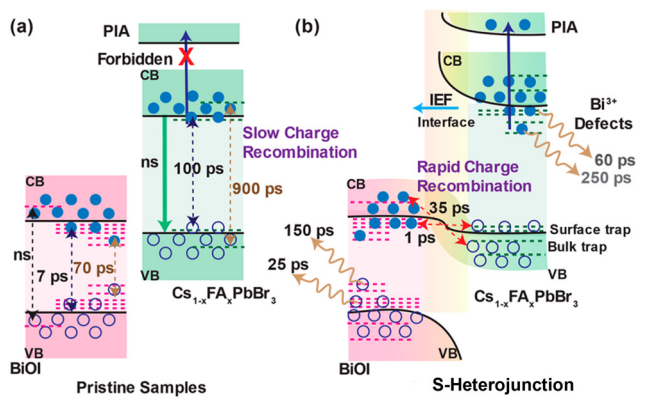

Fig. 6 (a) Depiction of kinetic models for (a) pristine BiOI and $Cs_{1-x}FA_xPbBr_3$ (CF) and (b) hybrid $Cs_{1-x}FA_xPbBr_3$: BiOI (CF : BiOI) heterojunction samples. IEF represents the internal electric field generated in the heterojunction. Reprinted with permission from ref. 106. Copyright 2022, American Chemical Society.

In another work, BiOI nanosheets and In_2O_3 were synthesized individually by the solvothermal technique.[107] Similar to the above work, a heterojunction was formed by mixing the as-synthesized semiconductors and heating solvothermally to obtain the heterojunction of BiOI/In_2O_3. The spherical morphology of In_2O_3 was decorated on the nanosheets. However, it was observed that the morphology was non-uniform throughout the heterojunction material. It can be inferred that the heterojunction fabricated *via* the solvothermal technique using the individual semiconductor materials resulted in the aggregation of In_2O_3 on BiOI nanosheets.[107] The BiOI/C_3N_4 constructed on hydrophobic carbon fiber paper *via* the electrophoretic deposition process exhibited significant selectivity for CO production during the CO_2 reduction reaction.[108] Initially, pre-formed g-C_3N_4 sheets and an iodine powder were dispersed in the acetone solvent, wherein protons were released upon the reaction of iodine with acetone. Later, BiOI/carbon fibers and Pt electrodes were used as the cathode and anode, respectively, which was followed by the application of an external potential.[108] The BiOI-nanosheets were vertically grown on the surface of carbon fibers, and g-C_3N_4 sheets completely wrapped the fibers to form 2D/2D contacts between the semiconducting surfaces.[108]

Li *et al.* carried out interfacial engineering with the formation of the p–n junction by compositing BiOI and Zn_2TiO_4.[109] The presence of oxygen vacancies sped up the CO_2 reduction process.[110] They extended the lifetime of the charge carrier and also acted as activation sites to enhance the adsorption of CO_2. Wang *et al.* fabricated a 2D/2D Bi_2MoO_6/BiOI S-scheme heterojunction to enhance the photoreduction of CO_2.[110] BiOI nanosheets were grown on few-layered Bi_2MoO_6 nanosheets using the solvothermal technique. The S-scheme mechanism was investigated by utilizing time-resolved photoluminescence spectroscopy, work function and charge density difference analyses. The nanosheets of Bi_2MoO_6 on BiOI nanospheres demonstrated that the van der Waals heterojunction is effective in accelerating the photogenerated charge carriers. The authors established that the charge transfer takes place from Bi_2MoO_6 to BiOI in addition to large-area van der Waals heterojunctions and S-scheme heterojunctions.[110]

Hongyu Fu *et al.* synthesized the heterostructure of Cu_2O and carbon-loaded BiOI using two-step methods.[111] The yield of methanol and ethanol from CO_2 was 722.8 μmol g^{-1} and 264.46 μmol g^{-1} for 8 h respectively. The photocatalytic performance of C–BiOI was significantly increased compared to pristine BiOI. The heterostructure of Cu_2O and carbon-loaded BiOI further improved the photocatalytic activity. Cu_2O is a p-type semiconductor with a band gap of 2.2 eV. Nanoparticles of Cu_2O were decorated onto the nanosheets of C–BiOI by the chemical deposition method. The introduction of Cu_2O

remarkably increased the photogenerated charge carriers and the surface area of the heterostructure, which provided more active sites for CO_2 reduction.[111]

BiOI-based 2D–2D heterojunction materials have been designed in order to elevate the photocatalytic performance. The band structures of C_3N_4 and BiOI are favourable to form S-heterojunctions, which can boost charge separation.[71] Li *et al.* proposed S-scheme charge transport, which increases the redox capability of both BiOI and C_3N_4 and converts CO_2 to CO.[112] The formation of the S-scheme heterojunction facilitates the electrons to move from C_3N_4 to BiOI, creating a depletion region in C_3N_4, whereas electron accumulation occurs in BiOI. In order to develop wide-wavelength-responding photocatalysts, the authors interfaced In_2O_3 with BiOI, because In_2O_3 exhibits a band gap of 2.8 eV, which falls in the visible region. It is also known to possess good electronic conductivity and is resistant to corrosion. The type-II heterojunction was fabricated by the solvothermal method.[107] In_2O_3/BiOI produced CO and CH_4.[72]

3.2 $BiVO_4$

As there is a larger difference in the reduction potential for CO_2 and the conduction band potential of $BiVO_4$, only few studies are available on the use of pure $BiVO_4$ in the photocatalytic reduction of CO_2. It has been found that $BiVO_4$ can selectively convert CO_2 to ethanol. In order to improve the photocatalytic performance, several strategies have been adopted such as morphological control, doping with metals and defect introduction.[56,113] It is found from the literature that metal nanoparticle deposition can effectively tune the band gap of $BiVO_4$ and thereby improve the selectivity and conversion efficiency.[113,114] High-performance $BiVO_4$ QDs with Au nanoparticles were fabricated and heterojunctioned with rutile nanorod arrays.[115] The

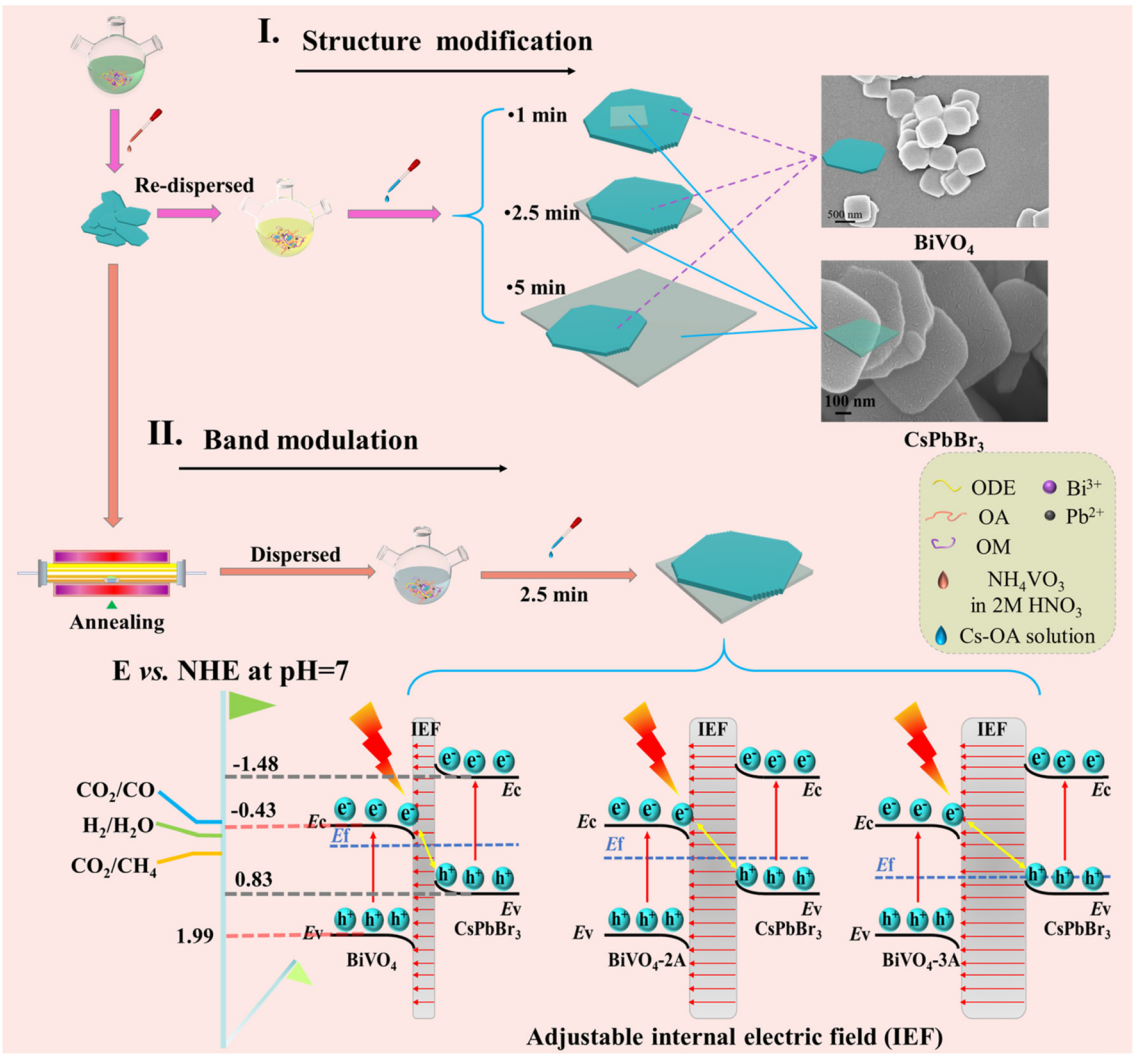

Fig. 7 Schematic of the synthesis, structural modification and band modulation of the $BiVO_4$/$CsPbBr_3$ heterojunction. Reprinted with permission from ref. 122. Copyright 2022, Elsevier.

surface plasmon resonance of Au not only helped in boosting the charge separation but also increased the light response of the photocatalyst.[116,117] This led to the prolonged lifetime of the charge carriers and the increased separation efficiency. A similar approach was adopted to construct Z-scheme $BiVO_4$–Au–Cu_2O, where $BiVO_4$ (010)–Au provides the Schottky junction and promotes electron extraction from $BiVO_4$.[118] In order to tune the electronic band structure of $BiVO_4$, Duan *et al.* co-decorated $BiVO_4$ with Ag and Bi nanoparticles.[119] The hollow microstructures of Bi/$BiVO_4$, which were synthesized by the solvothermal method, showed enhanced performance for the conversion of CO_2 to CO. To further improve photocatalytic reduction towards CO, metallic Ag nanoflakes were loaded on Bi/$BiVO_4$. The increased performance was mainly due to the extended visible light response and enhanced separation efficiency. Increased attention has been given to copper to substitute noble metals because it also increases the photocatalytic performance, as copper acts as a hole/electron mediator, which facilitates charge separation and improves the photocatalytic performance.[120] Wei *et al.* fabricated the composites of $BiVO_4$ and CdS and found an increase in the photocatalytic activity towards CO_2 reduction.[121]

2D-$BiVO_4$ has also been heterojunctioned with perovskites 2D-$CsPbBr_3$ to achieve high efficiency in CO formation without any co-catalysts or sacrificial agents (Fig. 7).[122] The preparation step involved the heterogeneous nucleation of $CsPbBr_3$-sheets on the surface of $BiVO_4$ *via* the annealing step in an inert atmosphere, which outlines the stability of $BiVO_4$ as the substrate surface. The presence of oxygen vacancies in $BiVO_4$ achieved a gradient Fermi level shift and enlarged the Fermi level gap between the semiconductors. This process was accompanied by an enhanced interfacial electric field in the heterojunction, which consecutively promoted the charge carrier separation process. It is interesting to note that pure $CsPbBr_3$ had a quasi-square morphology with random sizes, while uniform nanosheets were grown on the $BiVO_4$ substrate surface, which further emphasize the pivotal role of the substrate surface in altering the morphological features during the nucleation process.[122]

Wang *et al.* further explored the synthesis of the Bi_2S_3/$BiVO_4$ heterostructure, which was obtained from the *in situ* selective ion exchange method. The authors loaded the cocatalyst MnO_x on the heterojunction photocatalysts to improve the selectivity.[60] In this work, the photooxidation deposition method was adopted to decorate the MnO_x facet selectively. $BiVO_4$ was synthesized by the hydrothermal method, and Bi_2S_3 nanosheets were preferentially grown on (110) of $BiVO_4$. Bi_2S_3 was grown on (110) of $BiVO_4$ by sulfurization. As the concentration of S^{2-} ions increased, the surface of $BiVO_4$ turned rough as VO^{3-} ions were replaced by S^{2-} because the solubility of Bi_2S_3 was more than $BiVO_4$. It is worth noting that if the reaction time was less than 90 minutes, the crystallinity of Bi_2S_3 was poor and structurally unstable. Therefore, effective interfacial contact would be unsuccessful in the short duration of the reaction.[60] However, as the time duration increased to 120 minutes, the reaction would promote non-selective epitaxial growth. The sponge-like structure of MnO_x grew selectively on the (110) facets of $BiVO_4$ rather than on the (010) facets of Bi_2S_3 nanosheets.[60] The photocatalytic reduction of CO_2 to CH_3OH was observed in this heterostructure with a production rate of 20 ± 2.33 μmol g^{-1} h^{-1}.

The type-II heterojunction of $Bi_4Ti_3O_4$ with $BiVO_4$ was fabricated through a simple electrospinning technique and a solvothermal method.[123] $Bi_4Ti_3O_4$ with $BiVO_4$ formed a type-II heterojunction, which yielded various intermediates to give CO and CH_4OH (Fig. 8). A direct S-scheme heterojunction was formed between $BiVO_4$ and TiO_2, which changed the charge separation. Platinum decoration was carried out to enhance the CO_2 photoreduction. Platinum decoration on the surface of these catalysts helped in converting CO_2 to CH_4 by mitigating electron–hole pair recombination.[124]

An S-scheme heterojunction was fabricated by growing $BiVO_4$ on the surface of a metal–organic framework PCN-224 (Cu).[125] This photocatalyst exhibited 100% CO selectivity. Liu *et al.* decorated Co–Pi, a cocatalyst, on $BiVO_4/SnO_2$ and

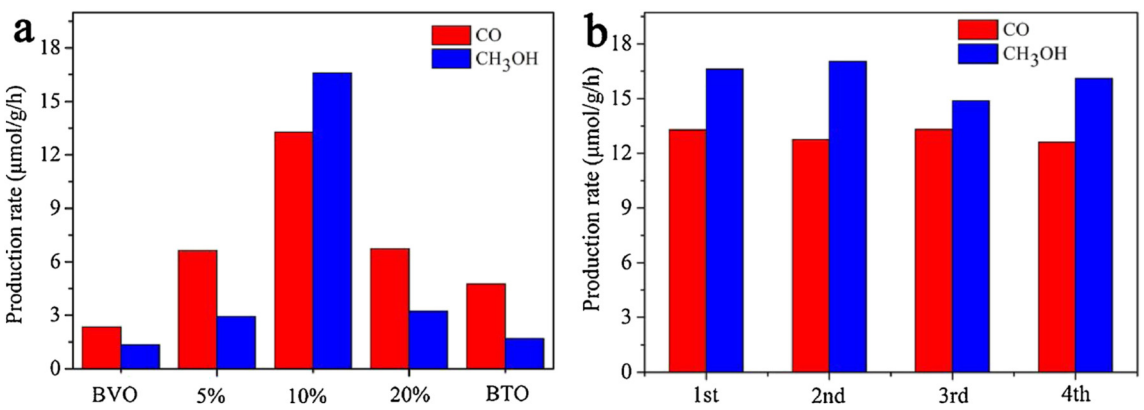

Fig. 8 (a) CH_3OH and CO evolutions on $BiVO_4/Bi_4Ti_3O_{12}$ with different $Bi_4Ti_3O_{12}$ contents and (b) photocatalytic activity stability of the $BiVO_4$/10% $Bi_4Ti_3O_{12}$ sample. Reprinted with permission from ref. 123. Copyright 2020, Elsevier.

coupled it with an Au cathode to achieve better conversion efficiency for CO_2.[126] The Z-schematic pathway for charge carriers was constructed using $SrTiO_3$:Rh and $BiVO_4$.[127] In this work, a powder of the photocatalyst was used without adjusting the pH. It is worth noting here that the conversion of CO_2 to CO was progressed without any addition of additives.

3.3 Bi_2WO_6

Bi_2WO_6, belonging to an Aurivillius family of oxides, has been widely researched for its photocatalytic activity owing to its structure, composition and electronic property. Owing to the presence of $[Bi_2O_2]$ and perovskite-type layers, Bi_2WO_6 possesses a narrow band gap, which is around 2.6 eV. Due to sluggish reaction kinetics and the high rate of recombination of photoinduced charge carriers, the photocatalytic performance is poor.[128] Therefore, in order to improve the photocatalytic activity, several modifications have been made to Bi_2WO_6 such as morphological control, heterojunction construction and doping.[129] It is important to have an update on the recent works on Bi_2WO_6 to design any new material or to modify the existing photocatalyst. As the band gap of Bi_2WO_6 is wider and unable to utilize the maximum visible light, heterojunctions have been constructed with other semiconductors such as $Cs_3Bi_2Br_9$, TiO_2, Cu_2O, $InVO_4$, C_3N_4, BiOBr and BiOI.[130–134]

NiO, with a narrow band gap of ~2.5 eV, which can efficiently absorb visible light, was composited with Bi_2WO_6, which gave an S-scheme charge transfer. The heterojunction yielded CO and CH_4 with 46.9 and 12.1 μmol g^{-1}, respectively, with the CO* intermediate.[135] Lulu Zhao *et al.* attempted to improve the selectivity of the catalyst towards CO from CO_2 by substituting Bi^{3+} and Ag^{+} ions *via* the liquid-phase exchange process.[136] The incorporation of Ag^{+} not only improved the adsorption of CO_2 and H_2O but also enhanced the separation of the charge carriers.[136] Ultrathin Bi_2WO_6 nanosheets with Ag^{+} and Bi^{3+} exhibited the conversion of CO_2 to CO with a yield of 116 μmol g^{-1} and with a selectivity of 95.7% after 6 h of the reaction without using any sacrificial agents. *In situ* DRIFT suggested that the intermediate formed was COOH*, which is then converted to thermodynamically stable CO*. It was possible to obtain methane *via* CO_2 photoreduction on Bi_2WO_6 by modifying the surface with surface plasmon resonance. Precisely controlling the oxygen vacancy in Bi–O–Bi and W–O–W led to high selectivity towards CH_4. The vacancy created an energy level that is very close to the conduction band, which helped in improving the life span of the charged carriers. To further improve the charge transport pathway, Bi_2WO_6 was covalently heterostructured with Bi_2O_3. The Bi_2O_3 nanosheets present on the Bi_2WO_6 surface rendered more active sites, which enhanced the adsorption of CO_2 on the surface.

Graphdiyne (GDY) is explored as a potential material for solar energy harvesting since its first synthesis.[137,138] An ultrathin heterojunction of GDY and Bi_2WO_6 was prepared by a simple hydrothermal method because GDY is an excellent material for efficient charge transfer.[139] Also, the increased surface area helped improve the CO_2 adsorption on the photocatalyst. GDY/Bi_2WO_6 yielded 2.13 and 0.23 μmol h^{-1} g^{-1} of CH_3OH and CH_4, respectively. The reduction of CO_2 yielded CH_3OH and CH_4 (Fig. 9).[139]

Further, to enhance the light absorption ability of the material, the hierarchical hollow structured heterojunction of Bi_2WO_6/TiO_2 was constructed by the *in situ* synthetic technique. This heterojunction interface generated the $Bi^{(3-x)+}$ active site, which could suppress the charge carrier recombination very effectively. In producing CO *via* CO_2 photoreduction, this heterojunction was better than that of pristine Bi_2WO_6 and Bi_2WO_6/TiO_2.[27] Similarly, Bi_2WO_6 was heterojunctioned with other semiconductors such as $InVO_4$, $La_2Ti_2O_7$, and ZnV_2O_6 either to improve the light absorption ability or to suppress the recombination rate of electron–hole pairs.[140–142]

Qiaoya Tang *et al.* constructed an S-scheme heterojunction of C_3N_4/Bi_2WO_6 using the electrostatic self-assembly

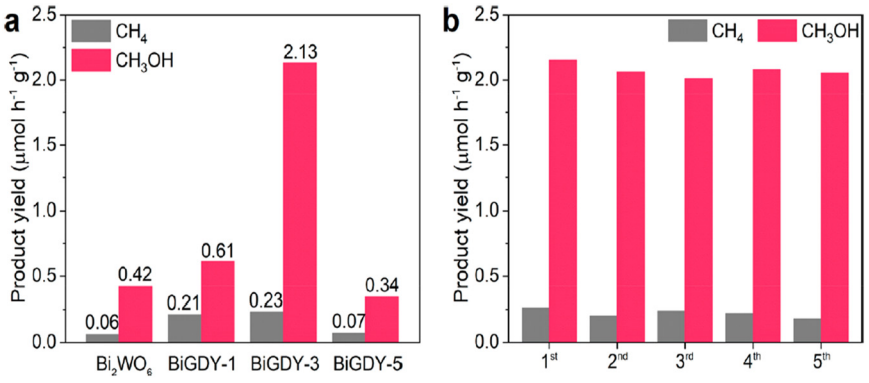

Fig. 9 (a) Photocatalytic CO_2 reduction performance of samples. (b) Cycling tests of the GDY/Bi_2WO_6 heterojunction (BiGDY). Reproduced with permission from ref. 139. Copyright 2021, American Chemical Society.

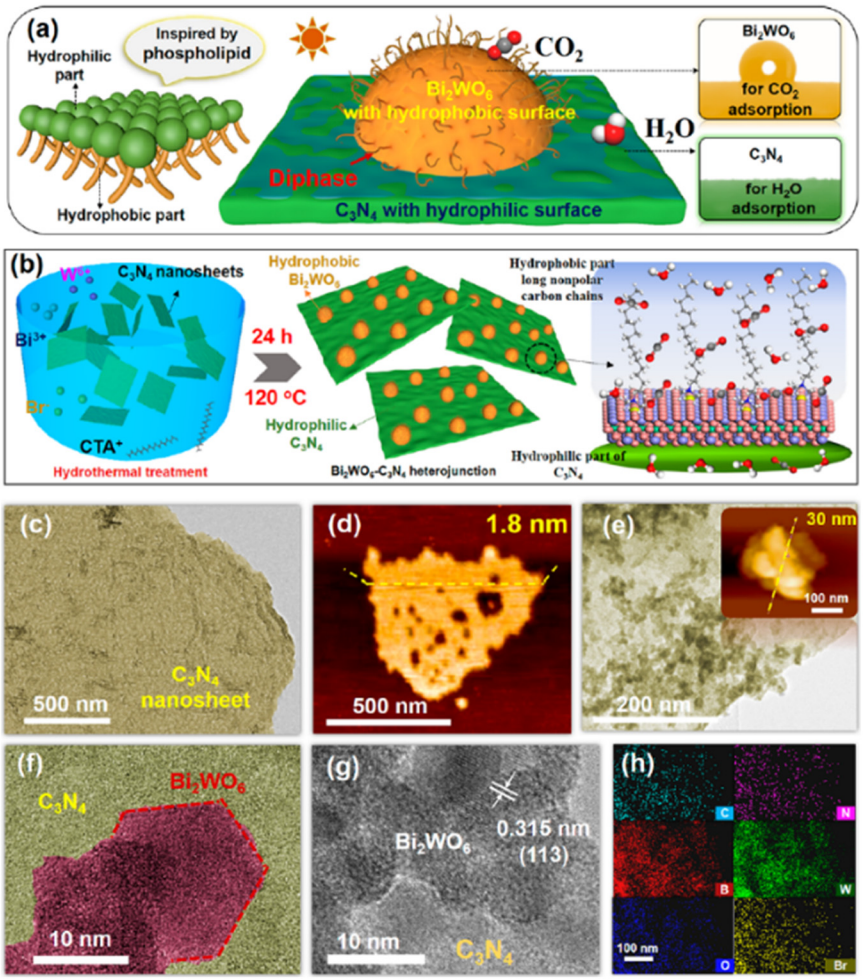

Fig. 10 (a) Schematic of the hydrophobic Bi_2WO_6–hydrophilic C_3N_4 photocatalyst and the distribution of CO_2 and H_2O. (b) Schematic of the preparation of a phospholipid-mimicking photocatalyst. (c) TEM image and (d) AFM image of C_3N_4. (e) TEM image and AFM image (inset) of Bi_2WO_6–CN. (f and g) HR-TEM images of Bi_2WO_6–C_3N_4. (h) EDS elemental mapping of Bi_2WO_6–C_3N_4. Reproduced with permission from ref. 144. Copyright 2024, American Chemical Society.

method.[143] The authors claimed that the formed ultrathin 2D/2D C_3N_4/Bi_2WO_6 heterostructure offers abundant reaction sites, which promote efficient charge transfer. Yunpeng Liu *et al.* introduced hydrophobic and hydrophilic ends in the diphasic photocatalyst to solve the competitive adsorption issue of CO_2 and H_2O. This amphipathic diphasic hydrophobic and hydrophilic photocatalyst not only inhibited the recombination of charge carriers but also could enrich CO_2 and H_2O on hydrophobic and hydrophilic surfaces, respectively, as depicted in Fig. 10.[144]

In an effort to improve the yield of CH_4 in CO_2 photoreduction, Yan-Yang Li *et al.* modified Bi_2WO_6 with chloride ions to study the influence of protons produced during the water oxidation on CH_4 generation.[145] The density functional theory confirmed the mappings of Bi_2WO_6–C_3N_4. The chloride ions present on the surface of Bi_2WO_6 nanosheets not only promoted water oxidation but also favoured the formation of the CHO* intermediate, which facilitated the formation of CH_4. Due to the presence of chloride ions on the surface, the rate of the oxidation half-reaction goes smoothly, which indirectly promotes the reduction half-reaction (CO_2 reduction).[145] As 2D/2D nanosheets provide a large specific surface area and rich active sites, Yong Jiang *et al.* fabricated the heterojunction of $CsPbBr_3/Bi_2WO_6$.[146] This enabled Z-scheme charge transfer and reduced charge carrier recombination to obtain the yields of 1582.0 μmol g^{-1} for CO and 8602 μmol g^{-1} of CH_4.[146]

Black phosphorous (BP) is a 2D material that is considered a potential candidate for photocatalytic applications because it provides a short diffusion length for the charge carriers. Because BP has a large specific area, it offers ample reaction sites for CO_2 adsorption. Therefore, BP has been used for constructing heterojunctions with Bi_2WO_6 because it is believed to accelerate the multistep electron process and dimerization of the C–C bond. Minghui Zhang *et al.* fabricated 2D/2D BP/Bi_2WO_6 by the electrostatic assembly method.[147] Organic oxidation to value-added products was coupled with CO_2 reduction, which lowered the

thermodynamic barrier for water oxidation. In this regard, benzylamine, which is a derivative of the renewable biomass, was used for organic oxidation to give imines as a high-value product. The adsorption study revealed that Bi_2WO_6 with BP exhibited more active sites for CO_2 adsorption. In addition to this, benzylamine provided alkaline media, which increased the solubility of CO_2 in the solution. *In situ* Fourier transform infrared (FTIR) suggested that CO* and CH_3^* were the intermediates for the conversion of CO_2 to C_2H_5OH.[136] To harvest visible light absorption and to improve charge transfer, g-C_3N_4 was introduced on Bi_2WO_6. The photocatalytic performance was further enhanced by incorporating reduced graphene oxide (rGO).[143,148] In another report, ultrathin 2D/2D Bi_2WO_6/g-C_3N_4 offered abundant contact interfaces with more accessible reaction sites that exhibited higher selectivity for CO generation compared to CH_4. The higher content of Bi_2WO_6 hampered the performance of the composite, as it could shield the incident photons striking the catalyst surface and hinder the bandgap excitation process. Furthermore, the composite retained its performance even after four consecutive cycles.[143] These 2D/2D heterojunctions with face-to-face interfaces could lower the intrinsic resistance and boost the charge carrier separation process.[149]

The deposition of QDs like $Cs_3Bi_2Br_9$ on the Bi_2WO_6-nanosheets could selectively promote the CO_2 reduction reactions to form CO under visible light.[134] This unique 0D/2D (dot-to-face) geometry and lead-free bismuth halide perovskite semiconductor remained as an added advantage for this composite. The larger surface area of 2D sheets enabled the finer distribution of QDs on their surface, which not only resulted in a stable heterojunction but also lowered the distance for the charge carrier migration process. The preparation method was flexible as it only involved the dispersion of positively charged QDs on the negatively charged Bi_2WO_6 sheets in isopropanol suspension through the electrostatic self-assembly approach. This strategy benefits from the prospect of retaining the pristine morphology of the concerned semiconductors during the heterojunction formation. The ESR analysis revealed the generation of both hydroxyl and superoxide radicals, which further confirmed the formation of the S-scheme heterojunction between them.[134]

3.4 Bi_2MoO_6

Bi_2MoO_6 is also found to be an interesting material that belongs to the Aurivillius oxide family. The structure of Bi_2MoO_6 consists of alternating arrays of $[Bi_2O_2]$ and $[MoO_6]$ octahedral layers. This ternary metal oxide is an *n*-type semiconductor possessing a narrow band gap that can utilize visible light of the solar spectrum.[150,151] It is possible to effectively tune the electronic distribution and morphology to optimize the photocatalytic application towards CO_2 reduction. By changing the temperature, reaction time and solvent, it is easier to modify the morphology of Bi_2MoO_6. Therefore, enormous efforts have been put into improving the photocatalytic performance of Bi_2MoO_6 by morphological control and heterojunction compositing.

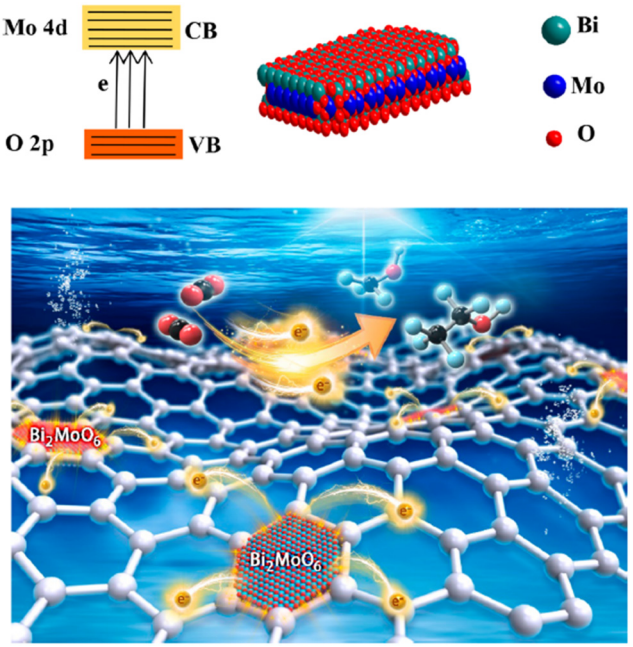

Fig. 11 Unit cell model of Bi_2MoO_6 and electron transfer. Reproduced with permission. Reprinted with permission from ref. 152. Copyright 2020, American Chemical Society.

Dai *et al.* grew Bi_2MoO_6 QDs on rGO scaffolds using an economically viable hydrothermal method.[152] Due to the high surface area of rGO, the dispersion of Bi_2MoO_6 QDs was enhanced. The electron migration from Bi_2MoO_6 QDs to rGO was facile because rGO exhibited excellent electrical conductivity. The photocatalytic mechanism is illustrated in Fig. 11.

Yu *et al.* fabricated a hierarchical heterostructure of 2D nanosheets of Bi_2MoO_6 grown on 1D In_2S_3 using the solvothermal technique. The hollow nanotubes of the In_2S_3 nanostructure were designed using the MIL-68 precursor. The surface oxygen vacancy was created by using *N*,*N*,*N*′,*N*′-tetramethylethylenediamine (TMEDA). However, the morphology of Bi_2MoO_6 nanosheets was distorted to give a particle-like morphology when TMEDA was used to introduce surface oxygen vacancies.[153] The presence of the interfacial Mo–S bond in Bi_2MoO_6/$ZnIn_2S_4$ boosted the production of CO from CO_2 reduction reactions.[151] The *in situ* loading of $ZnIn_2S_4$ nanoflakes on the porous microspheres of Bi_2MoO_6 under the solvothermal conditions offered plentiful catalytic sites for CO_2 adsorption and activation processes. Furthermore, the hierarchical structures enhanced the visible light absorption and possessed good photostability and reusability. The generation of superoxide and hydroxyl radicals, as confirmed from the ESR analysis, validated the formation of the S-scheme heterojunction between them.[151]

The oxygen-vacancy engineered Bi_2MoO_{6-x}/MoS_2 was active for CO_2 reduction to form CO, wherein oxygen vacancies were obtained from pristine Bi_2MoO_6 *via* a simple annealing step. It is interesting to note that the oxygen vacancies did not disrupt the microsphere-like morphology of the host matrix, and the density of oxygen vacancies increased upon composite formation with MoS_2-nanosheets. The presence of these oxygen vacancies lowered the bandgap of the host matrix and acted as effective electron sink to delay the recombination of charge carriers and also reduced the work function of the host matrix, which indirectly decreased the energy required for the electron transfer process.[154]

Maryam Ahmadi *et al.* heterojunctioned Bi_2MoO_6 with the benchmark photocatalyst TiO_2 to reduce the rate of recombination of photogenerated electron–hole pairs.[155] The synergistic effect was achieved by compositing Bi_2MoO_6 with TiO_2, as the band gap of both materials achieved a staggered configuration. Bi_2MoO_6 nanosheets were decorated with TiO_2 nanobelts by a simple solvothermal method. As cocatalysts acted as electron scavengers, Pt–Cu was decorated on the composite by the reduction method. It was noticed that the photoresponse of the photocatalyst increased, and 34.6 μmol g^{-1} of methane was obtained for Bi_2MoO_6/TiO_2. Once the Pt–Cu were loaded on the composite, methane production was increased further as the cocatalyst helped trap the electrons and reduce the recombination rate.[155]

Other metal oxide semiconductor materials have also been heterojunctioned such as a spinel compound $ZnFe_2O_4$, which produced CO and CH_4.[156] The S-scheme pathway helped in a slight improvement of the CO_2 reduction; the catalyst needs to be improved to achieve better photocatalytic performance. The 2D/2D $Bi_2MoO_6/Zn_3V_2O_8$, which formed an S-scheme, produced CO and CH_4.[157]

Nanosheets, belts, particles and spheres of Bi_2MoO_6 have been synthesized, but reports on the QDs of Bi_2MoO_6 are uncommon.[158–160] Weili Dai *et al.* anchored QDs of Bi_2MoO_6 on 2D rGO sheets, which act as an electron reservoir, helping boost CO_2 reduction. QDs Bi_2MoO_6/2D rGO produced 84.8 μmol g^{-1} of methanol and 57.5 μmol g^{-1} of ethanol, which are the highest among bismuth-based photocatalysts in the reduction of CO_2.[152] Further, the QDs of Bi_2MoO_6 were deposited on pomelo-peel derived carbon (CPP) to improve the photocatalytic property of the catalyst. The CPP possesses a high specific surface area and has excellent thermal conductivity. As the photothermal temperature increases, it not only enhances the migration rate of the electrons and holes but also promotes the adsorption of CO_2. Mingnv Guo *et al.* synthesized 0D/3D CPP-A/Bi_2MoO_6 to achieve a photothermal synergy to effectively utilize the solar spectrum.[161] As the temperature increases up to 100 °C, the migration ability is increased, and a C–O–Bi bridge is formed, which enhances the electron transfer at the interface. This work provides a solution for the bottleneck problem of poor charge carrier transport in photothermal catalytic activity.[161]

By combining both *n*-type semiconductors In_2S_3 and Bi_2MoO_6, an S-scheme was achieved to design an efficient photocatalyst. 2D nanosheets of Bi_2MoO_6 grown on 1D nanotubes of In_2S_3 reduced the carrier diffusion length. The Z-scheme heterojunctions such as Bi_2MoO_6/CdS and Bi_2MoO_6/CeO_2 have also been constructed to improve the charge carrier transport.[162,163] An S-scheme heterostructure can also be achieved from $ZnIn_2S_4$ decorated on Bi_2MoO_6, where the Mo–S bond at the interface helps in improving the photocatalytic activity.[151] S-scheme heterostructures can also be achieved from chalcogenides, especially with MnS. Diethylenetriamine (DETA) ammonia treated MnS hollow sphere heterostructured with plasmonic Bi enhanced CO_2 reduction rate of Bi_2MoO_6.[164] The presence of basic functional groups on DETA reduced the activation energy of acidic CO_2, whereas the surface plasmon effect from Bi produced hot electrons and decreased the recombination rate of charge carriers. This combined effect helped boost the CO_2 photocatalytic reduction reaction.

Table 1 illustrates the different interfacial engineering of bismuth-based materials with various other compounds and their respective CO_2 conversion products. The synthesis method and charge carrier pathway followed by the heterojunction are also mentioned. It is interesting to note that most of the bismuth-based materials are fabricated by wet chemical approaches such as hydrothermal and solvothermal methods. However, these techniques pose several challenges, as the materials' purity and morphology are sensitive to the synthesis temperature and reaction time. Therefore, the reproducibility of the structural–morphological features would be difficult for the large-scale synthesis.[165,166]

Other bismuth containing materials, such as $Bi_{12}O_{17}Br_2$/g-C_3N_4, $Bi_{12}O_{17}Cl_2$/g-C_3N_4, Bi_3NbO_7/g-C_3N_4, $SrBi_4Ti_4O_{15}$/Bi_2O_3, Cs_2CuBr_4/Bi_2O_3, $BiOIO_3$/CdS and $Bi/Bi_4V_2O_{11}$, are explored for CO_2 photocatalytic conversion.[176–183] In particular, the presence of interfacial Bi–N bonds and the nitrogen vacancy in $Bi_{12}O_{17}Br_2$/g-C_3N_4 achieved simultaneous tetracycline degradation and CO_2 reduction reactions.[177] In fact, the photocatalytic reduction of CO_2 was improved in the presence of tetracycline compared to rhodamine B and phenol molecules, which was attributed to the superior electron-donating ability of TC. The flower-like $Bi_{12}O_{17}Br_2$ were decorated on the defective g-C_3N_4 surface *via* the wet chemical approach. The presence of defects was important to drive the coupled photocatalytic reactions. It was proposed that $*CO_2$ was transformed to *COOH through a hydrogenation step, which upon further protonation yielded *CO, which was feasible for the desorption from the composite surface. This work is a classical illustration of win-to-win strategy to achieve both environmental and energy related issues.[177] Alternatively, $Bi_{12}O_{17}Cl_2$/g-C_3N_4 promoted the formation of CH_4 *via* two-

Table 1 Comparison of heterojunctions of bismuth-based materials and their photocatalytic conversion of CO_2 along with synthesis technique

Bismuth-based material	Preparation method	Nature of the heterojunction	Products: production rate in μmol g^{-1} h^{-1}	Ref.
BiOCl/BiOBr	Hydrothermal Temperature – 160 °C Time – 12 h	Type-I	CO: 7.353	84
Bi_2WO_6/TiO_2	Solvothermal	Type-II	CO: 43.7	27
$BiOCl/Bi_2WO_6$	Hydrothermal Temperature – 120 °C Time – 12 h	Type-II	CO: 6.63	76
$BiOBr/Bi_2S_3$	Hydrothermal Temperature – 180 °C Time – 2 h	Type-II	CO: 103 500	92
BiOBr/CoAl LDH	Hydrothermal Temperature – 160 °C Time – 12 h	Type-II	CO: 4.096 CH_4: 4.174	96
$BiOI/In_2O_3$	Hydrothermal method Temperature – 180 °C Time – 12 h	Type-II	CO: 11.98 CH_4: 5.69	107
$BiVO_4/Bi_4Ti_3O_{12}$	Hydrothermal Temperature – 160 °C Time – 21 h	Type-II	CH_3OH: 16.6 CO: 13.29	123
$BiVO_4/Bi_2S_3/MnO_3$	Selective epitaxial growth Temperature – 180 °C Time – 90 min	Z-scheme	CH_3OH: 20 ± 2.33	60
$BiOBr/HNb_3O_8$	Self-assembly ultrasonic dispersion for 30 min	Z-scheme	CO: 164.6	167
$g\text{-}C_3N_4$/BiOI/RGO	Hydrothermal method Temperature – 160 °C Time – 6 h	Z-scheme	CO: 21.85	168
Co-MOF/Bi_2MoO_6	Solvothermal, followed by the *in situ* growth method Temperature – 165 °C Time – 16 h	Z-scheme	CO: 19.76 CH_4: 8.24	169
$BiVO_4/Cu_2O$/Bi	Solvothermal Temperature – 120 °C Time – 6 h	Z-scheme	CH_4: 1.8 CO: 8.4	170
In_2O_3/Bi_2S_3	Hydrothermal, followed by ultrasonication Temperature – 180 °C Time – 24 h	Z-scheme	CO: 2.67	171
Quinacridone/$BiVO_4$	Self-assembly method Stirring for 1 h	Z-scheme	CO: 407 CH_4: 29	172
$BiOCl/C_3N_4$	Hydrothermal Temperature – 120 °C Time – 12 h	Z-scheme	CO: 45.33	173
BiOBr-(001)/Bi_2SiO_5/Bi	Solvothermal method Temperature – 190 °C Time – 12 h	S-scheme	CO: 234.05	74
$BiOBr/Bi_2WO_6$	Hydrothermal Temperature – 160 °C Time – 6 h	S-scheme	CO: 55.17	94
$BiOBr/Cu_2O$	Hydrothermal Temperature – 160 °C Time – 12 h	S-scheme	CH_4: 22.78	97
$BiOBr/CsPbBr_3$	Self-assembly process Overnight magnetic stirring in the dark	S-scheme	CO: 104.4 CH_4: 10.0	103
$BiVO_4/CsPbBr_3$	*In situ* colloidal growth method	S-scheme	CO: 103.5	122
$Cs_3Bi_2Br_9$/porous BiOCl	Dipping method Magnetic stirring for 1 h	S-scheme	CO: 25.5	174
$BiVO_4$/Cu–Bi	Solvothermal Temperature – 120 °C Time – 6 h	Oxygen vacancy	CO: 2.96	56
BiOCl/Br–O_V	Solvothermal Temperature – 160 °C Time – 10 h	Defects	CO: 7.37	175

Note: readers are requested to follow the respective references for more information.

electron and two-proton reaction pathways.[181] On the contrary, $Bi_3NbO_7/g\text{-}C_3N_4$ promoted the formation of CH_4 as the reduction pathway proceeded through the formation of CH_3O^* and CHO^* fragments.[178] Lee *et al.* reported that

CdS-nanorods/$BiOIO_3$-nanosheets (1D/2D) selectively generated CO and minor amounts of H_2 during the CO_2 reduction reactions, and the activity was retained even after four consecutive cycles.[182] The line interfacial contact between the integrated materials promoted the charge carrier lifetime with minimal recombination pathways.[184] A significant improvement in photocatalytic performance was noticed, yet these materials must be explored further to enhance the conversion of CO_2 to value-added products.

Conclusions and perspectives

The photocatalytic reduction of CO_2 into fuels and simple chemicals is a versatile approach that can simultaneously address environmental issues, carbon neutrality and energy demands. The high degree of chemical inertness of CO_2, sluggish dynamics of multi-electron reduction reactions and massive charge carrier recombination in single-phase photocatalytic active materials have driven the emergence of heterojunction photocatalysts. In this context, bismuth-based materials are found to be an interesting class of materials because they possess a narrow band gap and a favourable electronic structure for the photocatalytic CO_2 reduction reaction. Although notable progress has been achieved with Bi-based heterojunctions, the achieved efficiency is still far from satisfactory, as the presence of a single electric field may not always boost the charge carrier separation process. Thus, future research must essentially focus on the coupling of multiple electric fields, which will not only extend the carrier lifetime, but also allow their diffusion to react with the adsorbed species. Furthermore, designing and fabricating the hierarchical Bi-based heterojunctions comprising QDs, 1D, 2D and 3D forms would be even more advantageous from the perspective of improving the light harvesting capacity, surface reactions and charge carrier separation kinetics. In addition, some importance should be given to the preparation of NIR-responsive Bi-based materials, which would spotlight our interest in harvesting the complete solar spectrum for the photocatalytic reactions. From the viewpoint of charge carrier dynamics, steering the migration of charge carriers in a specific path without compromising their lifetimes requires a suitable interface during the fabrication of heterojunctions. Alongside, the coupling of the CO_2 reduction reaction with pollutant degradation, H_2O_2 generation and the synthesis of organic compounds will fulfil our dream of achieving a win-win strategy comprising energy and environmental aspects.

This review summarizes the interfacial engineering carried out for bismuth-based materials in recent years for CO_2 reduction. A large number of reported works have demonstrated that interfacial engineering helps effectively enhance the charge separation, light absorption and adsorption of CO_2 on the surface of the photocatalyst. However, the conversion efficiency is far from the efficiency required to implement in practical applications. Most of the interfacially engineered bismuth-based photocatalysts exhibit a rate of reduction of CO_2 less than 100 μmol g^{-1}. It is also noticed from the previous literature that the product obtained from the photocatalytic reduction reaction is carbon monoxide. Though bismuth based materials show promising results in photoelectrochemical water splitting, the photocatalytic activity towards CO_2 reduction is insignificant even after interfacial engineering with several other competent materials. Therefore, attention must be paid to enhance the photocatalytic activity of bismuth-based materials to meet the practical requirements for photocatalytic CO_2 reduction.

Conflicts of interest

Authors declare that there is no competing financial interest.

Data availability

No data were used in this article.

References

1 B. Kumar, M. Llorente, J. Froehlich, T. Dang, A. Sathrum and C. P. Kubiak, *Annu. Rev. Phys. Chem.*, 2012, **63**, 541–569.
2 T. Abbas, H. S. M. Yahya and N. A. S. Amin, *Energy Fuels*, 2023, **37**, 18330–18368.
3 R. Pang, K. Teramura, M. Morishita, H. Asakura, S. Hosokawa and T. Tanaka, *Commun. Chem.*, 2020, **3**, 137.
4 S. J. Cobb, S. Rodríguez-Jiménez and E. Reisner, *Angew. Chem., Int. Ed.*, 2024, **63**, e202310547.
5 U. Ulmer, T. Dingle, P. N. Duchesne, R. H. Morris, A. Tavasoli, T. Wood and G. A. Ozin, *Nat. Commun.*, 2019, **10**, 3169.
6 H. S. Shafaat and J. Y. Yang, *Nat. Catal.*, 2021, **4**, 928–933.
7 G. Gadikota, *Commun. Chem.*, 2021, **4**, 23.
8 B. Wang, S. Chen, Z. Zhang and D. Wang, *SmartMat*, 2022, **3**, 84–110.
9 D. H. Apaydin, *Isr. J. Chem.*, 2022, **62**, e202100085.
10 C. Zuo, Q. Su and X. Yan, *Processes*, 2023, **11**(3), 867.
11 S. S. Bhosale, A. K. Kharade, E. Jokar, A. Fathi, S.-M. Chang and E. W.-G. Diau, *J. Am. Chem. Soc.*, 2019, **141**, 20434–20442.
12 T. Zhao, J. Xiong, W. Li, G. Cheng and S. X. Dou, *Chem. Eng. J.*, 2025, **506**, 160313.
13 D. K. Chauhan, N. Sharma and K. Kailasam, *Mater. Adv.*, 2022, **3**, 5274–5298.
14 S. C. Shit, I. Shown, R. Paul, K.-H. Chen, J. Mondal and L.-C. Chen, *Nanoscale*, 2020, **12**, 23301–23332.
15 E. Gong, S. Ali, C. B. Hiragond, H. S. Kim, N. S. Powar, D. Kim, H. Kim and S.-I. In, *Energy Environ. Sci.*, 2022, **15**, 880–937.
16 T. Zhao, W. Zhang, J. Xiong, W. Li and G. Cheng, *Sep. Purif. Technol.*, 2025, **360**, 130849.

17 G. Yang, J. Xiong, M. Lu, W. Wang, W. Li, Z. Wen, S. Li, W. Li, R. Chen and G. Cheng, *J. Colloid Interface Sci.*, 2022, **624**, 348–361.
18 W. A. Thompson, E. Sanchez Fernandez and M. M. Maroto-Valer, *ACS Sustainable Chem. Eng.*, 2020, **8**, 4677–4692.
19 S. G. Kumar, R. Kavitha and C. Manjunatha, *Energy Fuels*, 2023, **37**, 14421–14472.
20 B. Tang and F.-X. Xiao, *ACS Catal.*, 2022, **12**, 9023–9057.
21 W. Huang, Q. Zhu, Y. Zhu, C. Chen and J. Shen, *Mater. Today Energy*, 2023, **38**, 101458.
22 Z. Dong, B. Li, Y. Zhu and W. Guo, *EES Catal.*, 2024, **2**, 448–474.
23 L. D. M. Torquato, F. A. C. Pastrian, J. A. L. Perini, K. Irikura, A. P. d. L. Batista, A. G. S. de Oliveira-Filho, S. I. Córdoba de Torresi and M. V. B. Zanoni, *Appl. Catal., B*, 2020, **261**, 118221.
24 S. Wang, G. Wang, T. Wu, Y. Zhang, F. Zhan, Y. Wang, J. Wang, Y. Fu and J. Qiu, *J. Mater. Chem. A*, 2018, **6**, 14644–14650.
25 K. R. Rao, S. Pishgar, J. Strain, B. Kumar, V. Atla, S. Kumari and J. M. Spurgeon, *J. Mater. Chem. A*, 2018, **6**, 1736–1742.
26 Y. Xiao, A. Abulizi, K. Okitsu and T. Ren, *J. Ind. Eng. Chem.*, 2023, **125**, 317–324.
27 W.-R. Liu, S. Yu, Z. Liu, P. Jiang, K. Wang, H.-Y. Du, Z.-Y. Hu, M.-H. Sun, Y.-L. Wang, Y. Li, L.-H. Chen and B.-L. Su, *Inorg. Chem.*, 2024, **63**, 6714–6722.
28 Y. Ma, X. Yi, S. Wang, T. Li, B. Tan, C. Chen, T. Majima, E. R. Waclawik, H. Zhu and J. Wang, *Nat. Commun.*, 2022, **13**, 1400.
29 A. Sharma, A. Hosseini-Bandegharaei, N. Kumar, S. Kumar and K. Kumari, *J. CO2 Util.*, 2022, **65**, 102205.
30 J. Wu, Y. Huang, W. Ye and Y. Li, *Adv. Sci.*, 2017, **4**, 1700194.
31 S. G. Kumar and L. G. Devi, *J. Phys. Chem. A*, 2011, **115**, 13211–13241.
32 X. Li, Y. Sun, T. Xiong, G. Jiang, Y. Zhang, Z. Wu and F. Dong, *J. Catal.*, 2017, **352**, 102–112.
33 S. M. Ghoreishian, K. S. Ranjith, H. Lee, H.-I. Ju, S. Zeinali Nikoo, Y.-K. Han and Y. S. Huh, *J. Hazard. Mater.*, 2020, **391**, 122249.
34 S. M. Ghoreishian, K. S. Ranjith, B. Park, S.-K. Hwang, R. Hosseini, R. Behjatmanesh-Ardakani, S. M. Pourmortazavi, H. U. Lee, B. Son, S. Mirsadeghi, Y.-K. Han and Y. S. Huh, *Chem. Eng. J.*, 2021, **419**, 129530.
35 S. M. Ghoreishian, K. S. Ranjith, M. Ghasemi, B. Park, S.-K. Hwang, N. Irannejad, M. Norouzi, S. Y. Park, R. Behjatmanesh-Ardakani, S. M. Pourmortazavi, S. Mirsadeghi, Y.-K. Han and Y. S. Huh, *Chem. Eng. J.*, 2023, **452**, 139435.
36 K. Sridharan, S. Shenoy, S. G. Kumar, C. Terashima, A. Fujishima and S. Pitchaimuthu, *Catalysts*, 2021, **11**(4), 426.
37 S. Chen, D. Huang, M. Cheng, L. Lei, Y. Chen, C. Zhou, R. Deng and B. Li, *J. Mater. Chem. A*, 2021, **9**, 196–233.
38 Y. Zhang, G. Zhang, J. Di and J. Xia, *Curr. Opin. Green Sustainable Chem.*, 2023, **39**, 100718.
39 R. He, D. Xu, B. Cheng, J. Yu and W. Ho, *Nanoscale Horiz.*, 2018, **3**, 464–504.
40 J. Z. Hassan, A. Raza, U. Qumar and G. Li, *Sustainable Mater. Technol.*, 2022, **33**, e00478.
41 S. S. M. Bhat and H. W. Jang, *ChemSusChem*, 2017, **10**, 3001–3018.
42 K. Xu, L. Wang, X. Xu, S. X. Dou, W. Hao and Y. Du, *Energy Storage Mater.*, 2019, **19**, 446–463.
43 D. Chen, Z. Xie, Y. Tong and Y. Huang, *Energy Fuels*, 2022, **36**, 9932–9949.
44 S. Wang, L. Wang and W. Huang, *J. Mater. Chem. A*, 2020, **8**, 24307–24352.
45 A. Kumar, P. Singh, A. A. P. Khan, Q. V. Le, V.-H. Nguyen, S. Thakur and P. Raizada, *Chem. Eng. J.*, 2022, **439**, 135563.
46 H. Sudrajat and M. Nobatova, *RSC Appl. Interfaces*, 2025, **2**, 599–619.
47 J. Low, J. Yu, M. Jaroniec, S. Wageh and A. A. Al-Ghamdi, *Adv. Mater.*, 2017, **29**, 1601694.
48 C. P. Prathibha, M. Srinivas and S. G. Kumar, *Inorg. Chem. Front.*, 2025, **12**, 2138–2181.
49 S. G. Kumar and K. S. R. K. Rao, *RSC Adv.*, 2015, **5**, 3306–3351.
50 A. Balapure, J. Ray Dutta and R. Ganesan, *RSC Appl. Interfaces*, 2024, **1**, 43–69.
51 S. Harrison and M. Hayne, *Sci. Rep.*, 2017, **7**, 11638.
52 W. Zhang, A. R. Mohamed and W.-J. Ong, *Angew. Chem., Int. Ed.*, 2020, **59**, 22894–22915.
53 A. Ghosh, A. Pramanik, S. Pal and P. Sarkar, *J. Phys. Chem. Lett.*, 2024, **15**, 6841–6851.
54 Q. Xu, L. Zhang, B. Cheng, J. Fan and J. Yu, *Chem*, 2020, **6**, 1543–1559.
55 R. Kavitha, C. Manjunatha, J. Yu and S. G. Kumar, *EnergyChem*, 2025, **7**, 100159.
56 L. Huang, Z. Duan, Y. Song, Q. Li and L. Chen, *ACS Appl. Nano Mater.*, 2021, **4**, 3576–3585.
57 T. Wei, H. Xiao, R. Niu, B. Xu, H. Li, X. Yan, Y. Li, H. Ou, B. Lin and G. Yang, *Chem. Eng. Sci.*, 2024, **292**, 120012.
58 K. Wang, T. Sun, H. Ma, R.-J. You, Z.-H. He, J.-G. Chen, H. Wang, W. Wang, Y. Yang, L. Wang and Z.-T. Liu, *Sep. Purif. Technol.*, 2024, **340**, 126786.
59 X. Li, J. Yu, M. Jaroniec and X. Chen, *Chem. Rev.*, 2019, **119**, 3962–4179.
60 M. Wang, S. Zeng, A. R. Woldu and L. Hu, *Nano Energy*, 2022, **104**, 107925.
61 A. E. Mesoudy, D. Machon, A. Ruediger, A. Jaouad, F. Alibart, S. Ecoffey and D. Drouin, *Thin Solid Films*, 2023, **769**, 139737.
62 C. Sushma and S. G. Kumar, *Inorg. Chem. Front.*, 2017, **4**, 1250–1267.
63 P. Qiu, H. Liu, G. Wang, C. Wang, Z. Huang, C. Huang, Y. Lai, C. Xing and K. Liang, *J. Water Process Eng.*, 2024, **68**, 106372.
64 S. Liu, J. Sun, G. Ren and X. Meng, *Mater. Sci. Semicond. Process.*, 2022, **137**, 106230.
65 S. G. Kumar and K. S. R. K. Rao, *Appl. Surf. Sci.*, 2017, **391**, 124–148.

66 Z. Ali, J. Ma, M. Hong and R. Sun, *J. Mater. Chem. A*, 2023, **11**, 3297–3314.
67 S.-S. Wang, X. Liang, Y.-K. Lv, Y.-Y. Li, R.-H. Zhou, H.-C. Yao and Z.-J. Li, *ACS Appl. Energy Mater.*, 2022, **5**, 1149–1158.
68 Y. Wang, E. Chen and J. Tang, *ACS Catal.*, 2022, **12**, 7300–7316.
69 F. Wang, J. Guo, L. Han, H. Shen, L. Zhu and S. Chen, *Chem. Eng. J.*, 2023, **478**, 147365.
70 Y. Shi, G. Zhan, H. Li, X. Wang, X. Liu, L. Shi, K. Wei, C. Ling, Z. Li, H. Wang, C. Mao, X. Liu and L. Zhang, *Adv. Mater.*, 2021, **33**, 2100143.
71 Y. Wang, H. Wang, L. Guo and T. He, *J. Colloid Interface Sci.*, 2023, **648**, 889–897.
72 S. Vinoth, W.-J. Ong and A. Pandikumar, *Coord. Chem. Rev.*, 2022, **464**, 214541.
73 T. L. Yusuf, B. O. Orimolade, D. Masekela, K. A. Adegoke, K. D. Modibane and S. S. Makgato, *Mater. Today Sustain.*, 2025, **30**, 101115.
74 X. Guan, X. Zhang, C. Zhang, R. Li, J. Liu, Y. Wang, Y. Wang, C. Fan and Z. Li, *J. Colloid Interface Sci.*, 2023, **644**, 426–436.
75 H. Jiang, W. Wang, L. Sun, T. Kong, Z. Lu, H. Tang, L. Wang and Q. Liu, *J. Catal.*, 2022, **416**, 1–10.
76 X. Zhao, Y. Xia, X. Wang, N. Wen, H. Li, X. Jiao and D. Chen, *Chem. Eng. J.*, 2022, **449**, 137874.
77 X. Liu, H. Zhang, X. Qiu, H. Ye, Y. Xie and Y. Ling, *Appl. Catal., A*, 2024, **671**, 119574.
78 H. Maimaitizi, A. Abulizi, D. Talifu and Y. Tursun, *Adv. Powder Technol.*, 2022, **33**, 103562.
79 W. Li, Y. Zhang, W. Ran, Y. Wang, F. Tian, F. Zhang, M. Xu, D. Zhang, N. Li and T. Yan, *Appl. Catal., B*, 2024, **351**, 123978.
80 Z. Huang, J. Wu, M. Ma, J. Wang, S. Wu, X. Hu, C. Yuan and Y. Zhou, *New J. Chem.*, 2022, **46**, 16889–16898.
81 Q. Liu, C. Bai, C. Zhu, W. Guo, G. Li, S. Guo, D. Kripalani, K. Zhou and R. Chen, *Adv. Sci.*, 2024, **11**, 2400934.
82 Q. Chen, S. Wang, B. Miao and Q. Chen, *J. Colloid Interface Sci.*, 2024, **663**, 1005–1018.
83 T. Xu, X. Su, Y. Zhu, S. Khan, D.-L. Chen, C. Guo, J. Ning, Y. Zhong and Y. Hu, *J. Colloid Interface Sci.*, 2023, **629**, 1027–1038.
84 Y. Wu, M. Xu, Y. Wang, B. Hu, Y. Xie and Y. Ling, *Appl. Catal., A*, 2024, **677**, 119708.
85 Y. Jiang, Y. Wang, Z. Zhang, Z. Dong and J. Xu, *Inorg. Chem.*, 2022, **61**, 10557–10566.
86 Y. Chen, F. Wang, Y. Cao, F. Zhang, Y. Zou, Z. Huang, L. Ye and Y. Zhou, *ACS Appl. Energy Mater.*, 2020, **3**, 4610–4618.
87 Q.-S. Wang, Y.-C. Yuan, X. Hu, D.-W. Jin, F.-K. Zhang, X.-J. Liu, J.-F. Deng, W.-G. Pan and R.-T. Guo, *Energy Fuels*, 2024, **38**, 4554–4565.
88 A. Nawaz, S. Goudarzi, M. A. Asghari, S. Pichiah, G. S. Selopal, F. Rosei, Z. M. Wang and H. Zarrin, *ACS Appl. Nano Mater.*, 2021, **4**, 11323–11352.
89 Z.-W. Zhang, R.-T. Guo, J.-Y. Tang, Y.-F. Miao, J.-W. Gu and W.-G. Pan, *J. CO2 Util.*, 2021, **45**, 101453.
90 T. Zhang, M. Maihemllti, K. Okitsu, D. Talifur, Y. Tursun and A. Abulizi, *Appl. Surf. Sci.*, 2021, **556**, 149828.
91 D. Liu, D. Chen, N. Li, Q. Xu, H. Li, J. He and J. Lu, *Angew. Chem., Int. Ed.*, 2020, **59**, 4519–4524.
92 Y. Xi, W. Mo, Z. Fan, L. Hu, W. Chen, Y. Zhang, P. Wang, S. Zhong, Y. Zhao and S. Bai, *J. Mater. Chem. A*, 2022, **10**, 20934–20945.
93 J. Ma, L. Xu, Z. Yin, Z. Li, X. Dong, Z. Song, D. Chen, R. Hu, Q. Wang, J. Han, Z. Yang, J. Qiu and Y. Li, *Appl. Catal., B*, 2024, **344**, 123601.
94 J. Wu, K. Li, S. Yang, C. Song and X. Guo, *Chem. Eng. J.*, 2023, **452**, 139493.
95 X. Wei, M. U. Akbar, A. Raza and G. Li, *Nanoscale Adv.*, 2021, **3**, 3353–3372.
96 Y. Lu, D. Wu, Y. Qin, Y. Xie, Y. Ling, H. Ye and Y. Zhang, *Sep. Purif. Technol.*, 2022, **302**, 122090.
97 C. Yan, M. Xu, W. Cao, Q. Chen, X. Song, P. Huo, W. Zhou and H. Wang, *J. Environ. Chem. Eng.*, 2023, **11**, 111479.
98 Z. Qian, L. Zhang, Y. Zhang and H. Cui, *Sep. Purif. Technol.*, 2023, **324**, 124581.
99 D. Qin, Y. Zhou, W. Wang, C. Zhang, G. Zeng, D. Huang, L. Wang, H. Wang, Y. Yang, L. Lei, S. Chen and D. He, *J. Mater. Chem. A*, 2020, **8**, 19156–19195.
100 J.-Y. Zhu, Y.-P. Li, X.-J. Wang, J. Zhao, Y.-S. Wu and F.-T. Li, *ACS Sustainable Chem. Eng.*, 2019, **7**, 14953–14961.
101 Z. Miao, Q. Wang, Y. Zhang, L. Meng and X. Wang, *Appl. Catal., B*, 2022, **301**, 120802.
102 H. Y. Yin, Y. F. Zheng and X. C. Song, *RSC Adv.*, 2019, **9**, 11005–11012.
103 Z. Zhang, L. Li, Y. Jiang and J. Xu, *Inorg. Chem.*, 2022, **61**, 3351–3360.
104 W. Sun, J. Liu, F. Ran, N. Li, Z. Li, Y. Li and K. Wang, *Dalton Trans.*, 2024, **53**, 14018–14027.
105 Z. Wang, B. Cheng, L. Zhang, J. Yu and H. Tan, *Sol. RRL*, 2022, **6**, 2100587.
106 A. H. Bhosale, S. Narra, S. S. Bhosale and E. W.-G. Diau, *J. Phys. Chem. Lett.*, 2022, **13**, 7987–7993.
107 N. Sun, M. Zhou, X. Ma, Z. Cheng, J. Wu, Y. Qi, Y. Sun, F. Zhou, Y. Shen and S. Lu, *J. CO2 Util.*, 2022, **65**, 102220.
108 C. Yang, Q. Zhang, W. Wang, B. Cheng, J. Yu and S. Cao, *Sci. China Mater.*, 2024, **67**, 1830–1838.
109 T. Li, R. Tao, Y. Wang, T. Yan, X. Fan and K. Liu, *J. Colloid Interface Sci.*, 2024, **655**, 841–851.
110 Z. Wang, B. Cheng, L. Zhang, J. Yu, Y. Li, S. Wageh and A. A. Al-Ghamdi, *Chin. J. Catal.*, 2022, **43**, 1657–1666.
111 H. Fu, T. Zhang, A. Abulizi, K. Okitsu and Y. Tursun, *Opt. Mater.*, 2023, **139**, 113790.
112 H. Li, D. Wang, C. Miao, F. Xia, Y. Wang, Y. Wang, C. Liu and G. Che, *J. Environ. Chem. Eng.*, 2022, **10**, 108201.
113 X. Liu, S. Gu, Y. Zhao, G. Zhou and W. Li, *J. Mater. Sci. Technol.*, 2020, **56**, 45–68.
114 J. H. Kim, G. Magesh, H. J. Kang, M. Banu, J. H. Kim, J. Lee and J. S. Lee, *Nano Energy*, 2015, **15**, 153–163.
115 Q. Shi, Z. Li, L. Chen, X. Zhang, W. Han, M. Xie, J. Yang and L. Jing, *Appl. Catal., B*, 2019, **244**, 641–649.
116 R. Kavitha and S. G. Kumar, *Chem. Pap.*, 2020, **74**, 717–756.

117 R. Kavitha and S. G. Kumar, *Mater. Sci. Semicond. Process.*, 2019, **93**, 59–91.
118 C. Zhou, S. Wang, Z. Zhao, Z. Shi, S. Yan and Z. Zou, *Adv. Funct. Mater.*, 2018, **28**, 1801214.
119 Z. Duan, X. Zhao, C. Wei and L. Chen, *Appl. Catal., A*, 2020, **594**, 117459.
120 Z. Zhu, C.-X. Yang, Y.-T. Hwang, Y.-C. Lin and R.-J. Wu, *Mater. Res. Bull.*, 2020, **130**, 110955.
121 Z.-H. Wei, Y.-F. Wang, Y.-Y. Li, L. Zhang, H.-C. Yao and Z.-J. Li, *J. CO2 Util.*, 2018, **28**, 15–25.
122 X. Yue, L. Cheng, J. Fan and Q. Xiang, *Appl. Catal., B*, 2022, **304**, 120979.
123 X. Wang, Y. Wang, M. Gao, J. Shen, X. Pu, Z. Zhang, H. Lin and X. Wang, *Appl. Catal., B*, 2020, **270**, 118876.
124 M. Ahmadi, S. M. Alavi and A. Larimi, *Surf. Interfaces*, 2024, **45**, 103908.
125 M. Xie, Q. Xu, T. Lv and H. Liu, *J. Alloys Compd.*, 2024, **977**, 173342.
126 L.-X. Liu, J. Fu, L.-P. Jiang, J.-R. Zhang, W. Zhu and Y. Lin, *ACS Appl. Mater. Interfaces*, 2019, **11**, 26024–26031.
127 S. Yoshino, K. Sato, Y. Yamaguchi, A. Iwase and A. Kudo, *ACS Appl. Energy Mater.*, 2020, **3**, 10001–10007.
128 X. Y. Kong, W. Q. Lee, A. R. Mohamed and S.-P. Chai, *Chem. Eng. J.*, 2019, **372**, 1183–1193.
129 S. Girish Kumar and K. S. R. K. Rao, *Appl. Surf. Sci.*, 2015, **355**, 939–958.
130 J. F. de Brito, C. Genovese, F. Tavella, C. Ampelli, M. V. B. Zanoni, G. Centi and S. Perathoner, *ChemSusChem*, 2019, **12**, 4274–4284.
131 K. Du, G. Li, J. Yang and S. Zhang, *Powder Technol.*, 2024, **439**, 119656.
132 J. Liu, T. Du, P. Chen, Q. Yue, H. Wang, L. Zhou and Y. Wang, *Appl. Surf. Sci.*, 2024, **664**, 160274.
133 A. Rana, Sonu, A. Sudhaik, A. Chawla, P. Raizada, A. K. Kaushik, T. Ahamad, S. Kaya, N. Kumar and P. Singh, *Ind. Eng. Chem. Res.*, 2024, **63**, 6960–6973.
134 Y. Feng, D. Chen, Y. Zhong, Z. He, S. Ma, H. Ding, W. Ao, X. Wu and M. Niu, *ACS Appl. Mater. Interfaces*, 2023, **15**, 9221–9230.
135 Z. Li, Z. Li, J. Liang, W. Fan, Y. Li, Y. Shen, D. Huang, Z. Yu, S. Wang and Y. Hou, *Sep. Purif. Technol.*, 2023, **310**, 123197.
136 L. Zhao, H. Hou, L. Wang, C. R. Bowen, J. Wang, R. Yan, X. Zhan, H. Yang, M. Yang and W. Yang, *Chem. Eng. J.*, 2024, **480**, 148033.
137 Y. Gong, L. Shen, Z. Kang, K. Liu, Q. Du, D. Ye, H. Zhao, X. A. Sun and J. Zhang, *J. Mater. Chem. A*, 2020, **8**, 21408–21433.
138 G. Li, Y. Li, H. Liu, Y. Guo, Y. Li and D. Zhu, *Chem. Commun.*, 2010, **46**, 3256–3258.
139 C. Yang, Y. Wang, J. Yu and S. Cao, *ACS Appl. Energy Mater.*, 2021, **4**, 8734–8738.
140 J. Li, Y. Zhao, M. Xia, H. An, H. Bai, J. Wei, B. Yang and G. Yang, *Appl. Catal., B*, 2020, **261**, 118244.
141 Y. Li, J. Jiang, C. Zhu, W. Feng, S. Han and L. Li, *J. Environ. Sci.*, 2025, **154**, 665–677.
142 J. Li, F. Wei, Z. Xiu and X. Han, *Chem. Eng. J.*, 2022, **446**, 137129.
143 Q. Tang, W. Tao, J. Hu, T. Gui, Z. Wang, Y. Xiao, R. Song, Y. Jiang and S. Guo, *ACS Appl. Nano Mater.*, 2023, **6**, 17130–17139.
144 Y. Liu, R. Zou, Z. Chen, W. Tu, R. Xia, E. I. Iwuoha and X. Peng, *ACS Catal.*, 2024, **14**, 138–147.
145 Y.-Y. Li, J.-S. Fan, R.-Q. Tan, H.-C. Yao, Y. Peng, Q.-C. Liu and Z.-J. Li, *ACS Appl. Mater. Interfaces*, 2020, **12**, 54507–54516.
146 Y. Jiang, H.-Y. Chen, J.-Y. Li, J.-F. Liao, H.-H. Zhang, X.-D. Wang and D.-B. Kuang, *Adv. Funct. Mater.*, 2020, **30**, 2004293.
147 M. Zhang, Y. Mao, X. Bao, G. Zhai, D. Xiao, D. Liu, P. Wang, H. Cheng, Y. Liu, Z. Zheng, Y. Dai, Y. Fan, Z. Wang and B. Huang, *Angew. Chem., Int. Ed.*, 2023, **62**, e202302919.
148 I. T. Chen, M.-W. Zheng, Y.-C. Pu and S.-H. Liu, *Int. J. Energy Res.*, 2022, **46**, 15198–15210.
149 J. Su, G.-D. Li, X.-H. Li and J.-S. Chen, *Adv. Sci.*, 2019, **6**, 1801702.
150 H. Wei, F. Meng, H. Zhang, W. Yu, J. Li and S. Yao, *J. Mater. Sci. Technol.*, 2024, **185**, 107–120.
151 J. He, J. Lin, Y. Zhang, Y. Hu, Q. Huang, G. Zhou, W. Li, J. Hu, N. Hu and Z. Yang, *Chem. Eng. J.*, 2024, **480**, 148036.
152 W. Dai, W. Xiong, J. Yu, S. Zhang, B. Li, L. Yang, T. Wang, X. Luo, J. Zou and S. Luo, *ACS Appl. Mater. Interfaces*, 2020, **12**, 25861–25874.
153 B. Yu, Y. Wu, F. Meng, Q. Wang, X. Jia, M. Wasim Khan, C. Huang, S. Zhang, L. Yang and H. Wu, *Chem. Eng. J.*, 2022, **429**, 132456.
154 Y. Liu, X. Kong, X. Guo, Q. Li, J. Ke, R. Wang, Q. Li, Z. Geng and J. Zeng, *ACS Catal.*, 2020, **10**, 1077–1085.
155 M. Ahmadi, S. M. Alavi and A. Larimi, *Inorg. Chem.*, 2023, **62**, 20372–20389.
156 Y. Zhou, W. Jiao, Y. Xie, F. He, Y. Ling, Q. Yang, J. Zhao, H. Ye and Y. Hou, *J. Colloid Interface Sci.*, 2022, **608**, 2213–2223.
157 S. Li, N. Hasan, F. Zhang, J.-S. Bae and C. Liu, *J. Colloid Interface Sci.*, 2023, **652**, 1533–1544.
158 Y. Zhang, S. Liu, X. Guo, H. Mikulčić, R. Xiao and X. Wang, *J. Photochem. Photobiol., A*, 2024, **447**, 115278.
159 Y. Zhu, R. Wu, J. Hui, Z. Zhang and S. Wei, *J. Alloys Compd.*, 2024, **1003**, 175609.
160 X. Bai, L. He, W. Zhang, F. Lv, Y. Zheng, X. Kong, D. Wang and Y. Zhao, *Nanomaterials*, 2023, **13**, 1569.
161 M. Guo, Z. Wang, X. Wu, J. Qiu, L. Gu and Z. Yang, *ACS Appl. Energy Mater.*, 2023, **6**, 2863–2876.
162 Y. Wu, J. Xiao, J. Yuan, L. Wang, S. Luo, Z. Zhang, X. Fu and W. Dai, *J. Colloid Interface Sci.*, 2024, **674**, 158–167.
163 Y. Xie, C. Qiu, L. Wang, Y. Wang, J. Zhang, J. Zhang, H. Wan and G. Guan, *Ceram. Int.*, 2024, **50**, 25161–25169.
164 L. Liu, K. Dai, J. Zhang and L. Li, *J. Colloid Interface Sci.*, 2021, **604**, 844–855.
165 S. G. Kumar and K. S. R. K. Rao, *Nanoscale*, 2014, **6**, 11574–11632.

166 M. Sahu and C. Park, *Mater. Today Sustain.*, 2023, **23**, 100441.
167 C. Zhou, X. Shi, D. Li, Q. Song, Y. Zhou, D. Jiang and W. Shi, *J. Colloid Interface Sci.*, 2021, **599**, 245–254.
168 X. Hu, J. Hu, Q. Peng, X. Ma, S. Dong and H. Wang, *Mater. Res. Bull.*, 2020, **122**, 110682.
169 S. Song, Z. Song, H. Han, K. Wei, W. Zhang, D. Liu, Q. Wang, C. Ma, S. Feng and X. Duan, *Appl. Catal., A*, 2024, **683**, 119834.
170 W. Wang, X. Feng, L. Chen and F. Zhang, *Ind. Eng. Chem. Res.*, 2021, **60**, 18384–18396.
171 M. Sun, K. Fan, C. Liu, T. Gui, C. Dai, Y. Jia, X. Liu and C. Zeng, *Langmuir*, 2024, **40**, 12681–12688.
172 X. Yu, F. Wen, F. Zhang, P. Yang, Y. Zhao, Y. Wu, Y. Wang and Z. Liu, *ChemSusChem*, 2020, **13**, 5565–5570.
173 Y. Sun, X. Qi, R. Li, Y. Xie, Q. Tang and B. Ren, *Opt. Mater.*, 2020, **108**, 110170.
174 H. Wang, H. Zhu, Y. Nie, X. Zhang and G. Xiang, *ACS Appl. Mater. Interfaces*, 2025, **17**, 39218–39225.
175 R. Fang, Z. Yang, Z. Wang, J. He, J. Qiu, J. Ran and R. Godin, *Fuel*, 2024, **367**, 131514.
176 X. Zhao, Z. Duan and L. Chen, *Ind. Eng. Chem. Res.*, 2019, **58**, 10402–10409.
177 X. Jia, J. Cao, H. Sun, X. Li, H. Lin and S. Chen, *Appl. Catal., B*, 2024, **343**, 123522.
178 K. Wang, X. Feng, Y. Shangguan, X. Wu and H. Chen, *Chin. J. Catal.*, 2022, **43**, 246–254.
179 S. She, B. Zhao, J. Wang, Z. Wei, X. Wu and Y. Li, *Sep. Purif. Technol.*, 2023, **309**, 123064.
180 H. Tang, X. Wang, C. Yao and Z. Zhang, *Sep. Purif. Technol.*, 2024, **338**, 126544.
181 Y. Huo, J. Zhang, Z. Wang, K. Dai, C. Pan and C. Liang, *J. Colloid Interface Sci.*, 2021, **585**, 684–693.
182 D.-E. Lee, N. Mameda, K. P. Reddy, B. M. Abraham, W.-K. Jo and S. Tonda, *J. Mater. Sci. Technol.*, 2023, **161**, 74–87.
183 P. J. Mafa, M. E. Malefane, A. O. Oladipo, S. L. Lebelo, D. Liu, J. Gui, B. B. Mamba and A. T. Kuvarega, *J. Environ. Chem. Eng.*, 2025, **13**, 117821.
184 S. Zhang, Y. Si, B. Li, L. Yang, W. Dai and S. Luo, *Small*, 2021, **17**, 2004980.